LIMNOLOGY and OCEANOGRAPHY: METHODS

Echo grid integration: A novel method for preprocessing multibeam water column data to quantify underwater gas bubble emissions

Peter Urban [1,2]* Mario E. Veloso-Alarcón [1] Jens Greinert [1,3]
[1]GEOMAR Helmholtz Centre for Ocean Research Kiel, Kiel, Germany
[2]Department of Geology and Department Data Analysis and Mathematical Modelling, Ghent University, Ghent, Belgium
[3]Christian-Albrechts University Kiel, Institute of Geosciences, Kiel, Germany

Abstract

Water column imaging multibeam echo sounder systems (MBESs) are a promising technology for quantitative estimates of the gas bubble volume flow within large gas seepage areas. Considerable progress has been made in recent years toward applicable calibration methods for MBESs as well as developing inversion models to convert acoustically measured backscattering cross sections to gas bubble volume flow. However, MBESs are still not commonly used for quantitative gas flow assessments. A reason for this is the absence of published processing methods that demonstrate how MBES data can be processed to quantitatively represent bubble streams. Here, we present a novel method (echo grid integration) that allows for assessing the aggregated backscattering cross section of targets within horizontal water layers. This derived value enables quantifying bubble stream gas flow rates using existing acoustic inversion methods. The presented method is based on averaging geo-referenced volume backscattering coefficients onto a high-resolution 3D voxel-grid. The results are multiplied with the voxel volume to represent measurements of the total backscattering cross-section within each voxel cell. Individual gridded values cannot be trusted because the beam pattern effects cause the values of individual targets to "smear" over multiple grid-cells. The true aggregated backscattering cross-section is thus estimated as the integral over the grid-cells affected by this smearing. Numerical simulation of MBES data acquisition over known targets assesses the method's validity and quantify it's uncertainty for different, realistic scenarios. The found low measurement bias (< 1%), and dispersion (< 5%) are promising for application in gas flow quantification methods.

Underwater gas bubble release is a worldwide phenomenon in oceans, seas, and lakes. It can be found at naturally occurring seep sites that are commonly found along shelfs and continental margins (e.g., Suess 2018), but also at man-made installations such as oil/gas wells and pipelines (e.g., Vielstädte et al. 2015). The released gas, typically methane but also carbon dioxide, can have a significant influence on the local marine ecosystem by providing methane as an energy resource and creating hard grounds through carbonate precipitation (Campbell 2006). In addition, such methane can end up in the atmosphere and—to a small percentage—contribute to global warming (e.g., Hornafius et al. 1999; Shakhova et al. 2010, 2014; Kirschke et al. 2013; Global Carbon Project 2021), can influence acidification (e.g., Biastoch et al. 2011; Pohlman et al. 2011) and might support deoxygenation (e.g., Boetius and Wenzhöfer 2013; Yamamoto et al. 2014) of our oceans.

Typical forms of submarine gas seepage are distinct gas bubble release vents, which emit continuous or temporally active bubble streams into the water column (e.g., Leifer et al. 2004; Greinert 2008; Schneider von Deimling et al. 2010; Bayrakci et al. 2014). Such bubble streams can be found and studied even at great water depth using active acoustic systems such as single beam echo sounder systems (SBESs; e.g., Hornafius et al. 1999; Greinert et al. 2006; Ostrovsky et al. 2008; Veloso-Alarcón et al. 2019) and/or MBESs (see Colbo et al. 2014 and following paragraph). Of these two widely used active acoustic system types, MBESs highly outperform SBESs with respect to seafloor and water

*Correspondence: peter.urban@ugent.be

column coverage (e.g., SBES beam width typically $\sim 7°$; MBES swath opening angle typically $\sim 120°$).

This difference makes MBESs a good tool for finding and mapping seep areas (Nikolovska et al. 2008; Gardner et al. 2009; Weber et al. 2012; Dupré et al. 2015; Römer et al. 2020), counting gas release vents (e.g., Sahling et al. 2014; Weber et al. 2014; Römer et al. 2017) and to support advanced 3D interpretations of gas bubble streams (e.g., Schneider von Deimling et al. 2015; Wilson et al. 2015; Li et al. 2020; Tréhu et al. 2021). In recent years, semiautomated and even fully automated methods have been developed to increase the potential of finding gas bubble streams in large MBES datasets (e.g., Schneider von Deimling and Papenberg 2012; Urban et al. 2016; Zhao et al. 2017; Zwanzig 2018; Xu et al. 2020; Weber 2021). However, methods that use MBESs for quantitative assessments of the detected underwater seepage are currently not as advanced as methods that use scientific SBESs (e.g., Ostrovsky 2009; Muyakshin and Sauter 2010; Leblond et al. 2014; Veloso et al. 2015; Padilla et al. 2019; Weidner et al. 2019; Li et al. 2020).

Scandella et al. (2016) used a method for computing gas flux from a stationary, horizontally looking MBES in lakes. Their method includes assumptions about static overlap of the acoustic samples and is therefore only suitable for statically placed observatories, but not for analyzing MBES data acquired with a moving vessel. Urban et al. (2016) published a method to create "acoustic flare maps" from MBES water column images (WCIs), which allows for a qualitative comparison of the received signal amplitudes from bubble streams. However, the authors did not investigate if and how such acoustic flare maps could be used for quantitative estimates of the mapped bubble streams. Multiple authors have extrapolated camera—or SBES—based quantifications toward the number of acoustic flares detected in WCI data (e.g., Sahling et al. 2014; Weber et al. 2014; Römer et al. 2017; Turco et al. 2022). While these are reasonable and effective approaches, they do not integrate the heterogeneous signal strength of the acoustic flares in the MBES data, leading to an extrapolation error that is difficult to quantify. Leifer et al. (2017) compared the acoustic signals received by a MBES from an artificially created bubble source and fitted a depth dependent calibration factor for converting the received data to gas fluxes. Their extensive work highlights the enormous number of practical challenges and factors to consider for such a conversion; but little methodological details are given on the exact processing of the acoustic raw data.

These details, and how they influence the reliability of gas flow quantification, are the topic of this work. To the best of our knowledge, no comprehensive method for processing MBES echo amplitudes to reach quantitative estimates of gas flow has so far been described in the accessible literature. We therefore investigated the basic sampling principles of a MBES water column survey to derive a new quantitative processing method, which we call echo grid integration. This method is based on averaging geo-referenced, measured volume backscattering coefficients from an MBES onto a regular voxel grid

(similar to Urban et al. 2016). The gridded measurements are multiplied with the voxel volume to represent a measurement of the total backscattering cross-section within each voxel-cell. These individual gridded measurements are erroneous because the beam pattern and pulse overlap cause the acoustic response of individual targets to "smear" over multiple grid-cells. The true aggregated backscattering cross-section of targets within this grid is therefore estimated as the integral over-all grid-cells that are affected by this smearing.

For simplification, we assume a calibrated MBES that can provide real target- and volume backscattering strength values in the description of this method. The challenges of calibrating a MBES and the applicability of our method toward uncalibrated MBESs are described in the comments and recommendation section.

It should be noted that this work does not focus on investigating the different acoustic inversion techniques in detail. Rather, we present a method for preprocessing the WCI data in such a way that correct backscattering cross section values of single bubbles and bubble streams are derived. Only such correctly derived data allow for applying quantification methods (model inversion or direct calibration) as they have previously been used for SBES data (comments and recommendations section 5.4).

The performance of the proposed method is assessed by a numerical simulation of the MBESs data acquisition over targets of known backscattering cross-section in different, realistic survey scenarios. The results from this error assessment are used to derive guidelines for choosing processing parameters and designing a good MBES gas flow quantification survey.

Similar simulations have previously been used to investigate uncertainties of echo integration methods for biomass estimations (e.g., Diner 2001, 2007; Holmin et al. 2012, 2016; ICES 2021 Annex 17). However, to the best of our knowledge, this is the first time that a numerical simulation is used to assess uncertainties associated with acoustically quantifying underwater bubble seepage.

Materials and procedures

Gas flow quantification of bubble streams using acoustic inversion

Acoustic inversion in the context of this work describes techniques for inverting the backscattering cross section σ_{bs} of (gas bubble) targets in the water column to physical properties of the target. For single targets, σ_{bs} can be measured using calibrated active acoustic systems by inverting the sonar equation (Urick 1996):

$$\text{EL}_a = \text{SL} - 2\text{TL}(R_a) + \text{TS}_a \tag{1}$$

$$\text{TS}_a = 10\log(\sigma_{bs;a}) \tag{2}$$

$$\text{TL}(R_a) = \alpha R_a + 20\log(R_a) \tag{3}$$

where,

EL_a	Target echo level caused by target a (dB re μPa at 1 m distance from the transducer)
SL	Transmitted source level (dB re μPa² m² at 1 m distance from the transducer)
$TL(R)$	Transmission loss associated with specific range R (dB re m²)
R_a	Range of target a from the transducer (m)
TS_a	Target strength of target a (dB re m²)
$\sigma_{bs;a}$	Backscattering cross section of target a (m²)
α	Logarithmic absorption coefficient (dB m^{-1})

For simplification, we here assume spherical targets such that the property $\sigma_{bs;a}$ is independent of the acoustic incidence angle. If it is known that a received echo level has been caused by a single spherical bubble, σ_{bs} can be used to compute the bubble radius/gas volume by inverting a spherical bubble model (e.g., Anderson 1950; Thuraisingham 1997; Ainslie and Leighton 2011; Li et al. 2020). However, the received target echo level alone does not allow for distinguishing if it was caused by a bubble or another type of target.

For bubble streams, the shape of the "acoustic flare"—which is the acoustic representation of the bubble streams in an echogram—can be used to detect and separate the related acoustic signals from other targets (e.g., Veloso et al. 2015 for SBESs; Urban et al. 2016 for MBESs). Since the individual bubbles of a bubble stream are usually too close to be acoustically separated, their acoustic return signals superpose on the measured signal. For simplification, we assume that multiple scattering (e.g., De Rosny and Roux 2001), target induced acoustic absorption (e.g., Toresen 1991) and coherent interferences between the returned acoustic signals (e.g., Gorska and Chu 2005) are neglectable. Under these assumptions, the total target echo level received from multiple bubbles at similar range can be approximated as integral over the individual echo contributions ("echo integration assuming perfect linearity", see e.g., Foote 1983; Simmonds et al. 2005):

$$EL_T = 10\log\left(\sum_{a \in T} 10^{\frac{EL_a}{10}}\right) \qquad (4)$$

where,

EL_T	Total target echo level received by multiple ensonified targets (dB re μPa²; 1 m distance from the transducer)
T	Set of targets that have been ensonified and contribute to EL_T

To enable gas flow estimates from recorded echo levels, the data must be processed to represent the aggregated backscattering cross section of all bubbles within an ensonified water column (EWC) layer ($\sigma_{AG;BL}$, Fig. 1). This value can then be inverted toward the gas volume flow rate of the bubbles passing through this layer using existing model inversion approaches
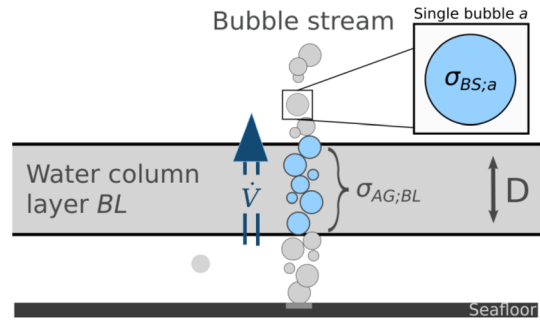

Fig. 1. $\sigma_{AG;BL}$ represents the aggregated backscattering cross section of the bubbles from a bubble stream within the water column layer BL of size D. It can be used to estimate the flow rate $\left(\dot{V}\right)$ of the bubble stream using different methods (see comments and recommendations sections).

or empirical direct calibration against bubble streams of known flow rates (see comments and recommendations sections 5.4).

To investigate how MBES data can be processed to represent $\sigma_{AG;BL}$, we here examine the basic principles of how MBES WCI surveys sample targets in the water column.

A simple forward model for water column imaging MBESs

Most MBESs use a mills-cross configuration (e.g., Clarke 2006; Lurton 2010). The systems emit an acoustic pulse of a certain duration that ensonifies a swath that is wide open in the across-track direction and narrow in the a long-track direction (Fig. 2). The angular shape of the transmitted power into the water column is called transmit beam pattern (B_{tx}^2). The MBES forms a set of receive beams that are steered in different angular directions and together form a fan along the across track direction below the vessel (Fig. 2). Each beam has a receive beam pattern $\left(B_{rx;bn}^2\right)$ that—in opposite to the transmit beam pattern—is narrow in the across-track direction but wide in the along-track direction (Fig. 2). For investigating targets that are far away from the transducer, the receive- and transmit unit can be seen as one monostatic transducer unit. The two-way beam pattern (beam response function) of this transducer unit can then be described as the product of the transmit- and receive beam pattern:

$$BF_{bn}(\theta, \varphi) = B_{tx}^2(\theta, \varphi) \times B_{rx;bn}^2(\theta, \varphi) \qquad (5)$$

where,

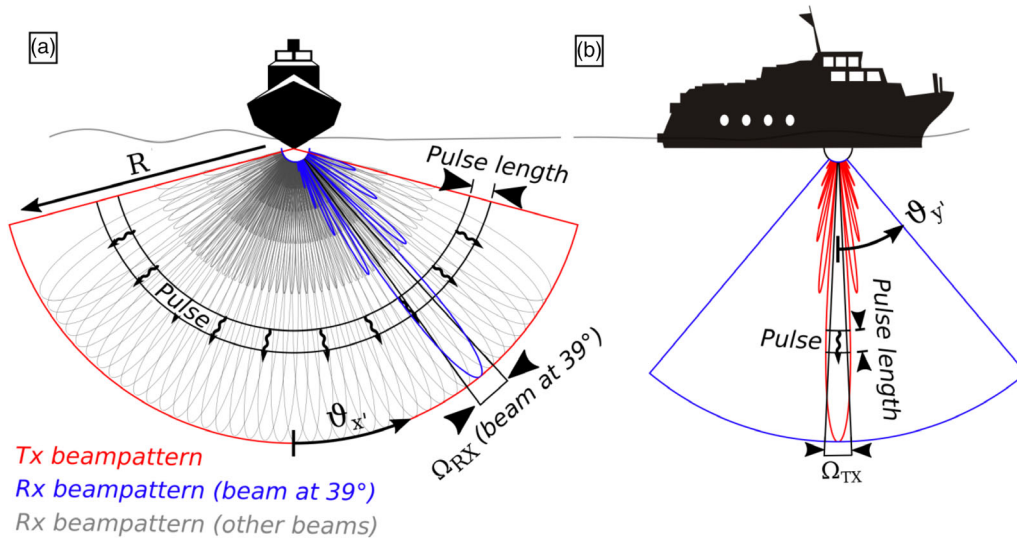| BF_{bn}	Beam response function of beam b_n (dimensionless)
θ	Polar angle (rad)
φ	Azimuthal angle (rad)
B_{tx}^2	Beam pattern of the transmit unit (dimensionless)
$B_{rx;bn}^2$	Beam pattern of the receive unit for beam b_n (dimensionless)

Fig. 2. MBES operating in mills-cross setup. (**a**) View from front. The transmitted pulse ensonifies a wide swath (red) in across-track direction, while the receive beams only cover a narrow angular fraction (blue and gray) of the across-track water column. (**b**) View from side: In a long-track direction, the receive beams receive signals in a wide opening angle (blue) while the transmitted pulse only covers a very narrow part of the water column (red). Ω values describe the beam Tx and Rx equivalent one-way beam angles (Eqs. 15 and 16).

BF_{bn} describes the sensitivity of a specific beam toward targets at a specific angular position relative to the transducer. For simplification, the transmit- and receive-beam pattern are here approximated to be perfectly isotropic in the across-track and along-track direction, respectively. This allows for expressing BF_{bn} using the transmit and receive beam pattern as two orthogonal components (for angle definitions/conversions see Supporting Information Data S1):

$$BF_{bn}\left(\vartheta_{a;y'},\vartheta_{a;x'}\right) = B_{tx0}^2\left(\vartheta_{a;y'}\right) \times B_{rx0;bn}^2\left(\vartheta_{a;x'}\right) \quad (6)$$

where,

$\vartheta_{a;y'}$	Along-track angle of target a within the transmit beam pattern (Fig. 2a; Supporting Information Data S1) (rad).
$\vartheta_{a;x'}$	Across-track angle of targe a within the receive beam pattern (Fig. 2b; Supporting Information Data S1) (rad).
B_{tx0}^2	Transmit beam pattern (isotropic in $\vartheta_{x'}$ direction) (dimensionless)
$B_{rx0;bn}^2$	Receive beam pattern (isotropic in $\vartheta_{y'}$ direction) (dimensionless)

The time that the acoustic pulse needs to travel to a target at a specific range (R) and back to the transducer (two-way travel time) can be computed using the known speed of sound underwater (c):

$$t_{2R} = 2 \times \frac{R}{c} \quad (7)$$

where,

t_{2R}	Two-way travel time for target at range R (s)
R	Range from transducer (m)
c	Speed of sound underwater (m s^{-1})

To create a WCI, the MBES samples the received acoustic signal at a constant time interval (sampling rate) typically until the seafloor is observed in the outer beams. Eq. 7 allows for associating the sampling time points (t_{sn}) of each acoustic sample with a range from the transducer (Fig. 8). Because of the limited length of the transmitted pulse, each acoustic sample acts as a range filter for targets in the water column. The sensitivity of an acoustic sample toward targets at range R is thereby determined by the transmitted pulse envelope (p_{env}) and the difference between the t_{sn} and the two-way travel time associated with R:

$$RF_{sn}(R) = p_{env}^2(\Delta t_{sn,2R}) \quad (8)$$

$$\Delta t_{sn,2R} = t_{sn} - t_{2R} \quad (9)$$

where,

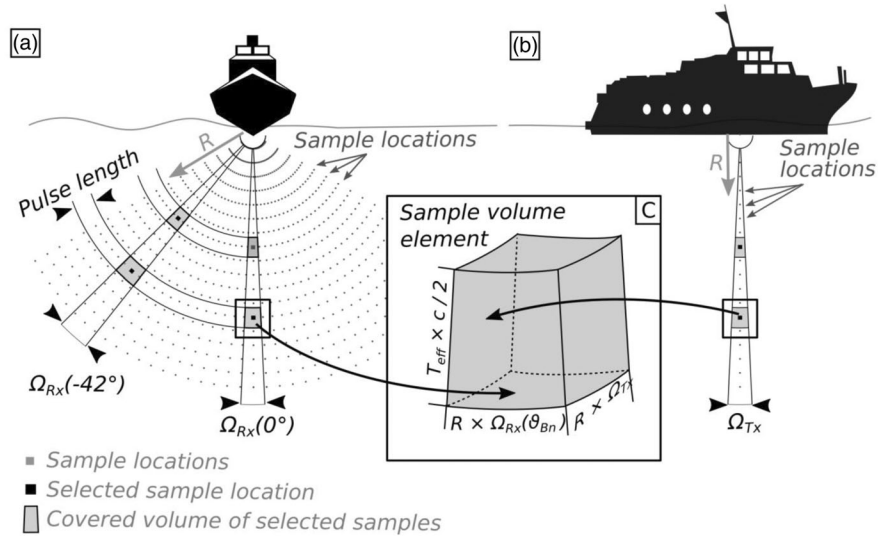|	
$RF_{sn}(R)$	Range response function for sample sn as a function of R (dimensionless)
$p_{env}(\Delta t_{sn,2R})$	Pulse envelope as function of time (dimensionless)
$\Delta t_{sn,2R}$	Time difference between t_{sn} and t_{2R} (s)
t_{sn}	Sampling time of sample sn (s)

Fig. 3. MBES sample locations and sample volumes of four selected example samples (**a,b**). The sample volumes are simplified to the exact shape described by the pulse length, the transmit and receive equivalent two-way beam angles, and the respective sample range (**c**).

The MBESs records an acoustic sample value for each sampling time point for each beam. The total set of all acoustic samples along all beams of one ping is called MBES WCI (Fig. 3). To distinguish between different acoustic samples, we define a three-dimensional sample index pn, sn, bn, which relates to the sample of ping number pn, sample number sn, and beam number bn, respectively (Fig. 4).

Calibrated MBES can account for the acoustic sensitivity of the transducer and for internal gains such that the received raw acoustic sample values can be converted to a calibrated, recorded echo level for each sample ($EL_{pn,sn,bn}$). Under the same assumptions made for Eq. 4 and neglecting noise and reverberation, $EL_{pn,sn,bn}$ is equal to the sum of the individual recorded echo level contributions ($EL_{a;pn,sn,bn}$) from all targets in the water column.

$$EL_{pn,sn,bn} = 10\log\left(\sum_{a \in A} 10^{\frac{EL_{a;pn,sn,bn}}{10}}\right) \tag{10}$$

where,

$EL_{pn,sn,bn}$	Total echo level recorded by the sample pn, sn, bn (dB re μPa² at 1 m distance from the transducer)
$EL_{a;pn,sn,bn}$	Target echo level contribution of individual target a to sample pn, sn, bn (dB re μPa² at 1 m distance from the transducer) (Eq. 11)
A	Set of all targets in the water column

The individual contribution of a target a toward a specific sample pn, sn, bn is equal to the echo level contribution (Eq. 1) filtered by the beam- and range-response functions of the respective sample (Eqs. 6 and 8):

$$EL_{a;pn,sn,bn} = EL_{pn;a} + 10\log\left(BF_{bn}\left(\vartheta_{pn;a;y'}, \vartheta_{pn;a;x'}\right)\right) \\ + 10\log\left(RF_{sn}\left(R_{pn;a}\right)\right) \tag{11}$$

where,

$EL_{pn;a}$	Target echo level for target a (Eq. 1) for the transducer position at ping number pn (dB re μPa² at 1 m distance from the transducer)
pn, sn, bn	Index of sample at ping number pn, sample number sn and beam number b_n
$R_{pn;a}$	Range of target a to the transducer for ping number pn (m)
$\vartheta_{pn;a;y'}$	Along-track angle of target a, at ping number pn (°)
$\vartheta_{pn;a;x'}$	Across-track angle of target a, at ping number pn (°)

In this work, Eqs. 6–11 are used to describe and simulate MBES WCI data using synthetic targets of known position and backscattering strength (forward modeling, see assessment section). The reverse processing—to estimate the backscattering cross-sections of targets using multibeam data—is described in the following sections.

Echo integration for individual MBES samples

Inverting Eqs. 6–11 to compute the backscattering cross section of the targets that caused a specific received echo level is difficult because the exact position of the targets is unknown such that the influence of the beam-/pulse-response functions cannot be corrected.

To reach an approximate inversion for individual samples, we compute the volume backscattering coefficient (s_V), which is defined as the sum of all discrete backscattering cross sections within the acoustically sampled volume divided by the size of this volume (Maclennan et al. 2002):
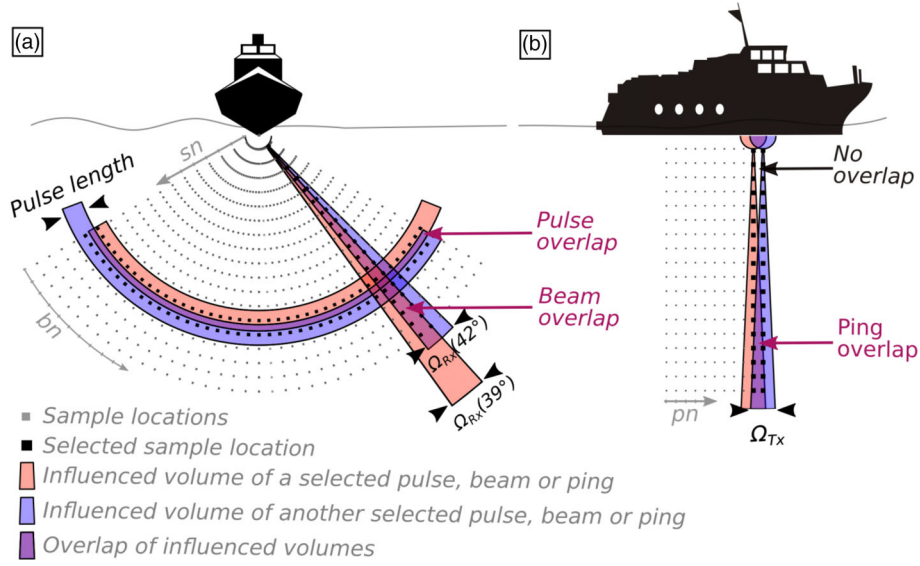
Fig. 4. MBES samples and sample volume overlap. (**a**) Front view, the samples of an individual ping are distributed in the water column at regular range (sample *sn*) and at regular angular distance (beam nr. *bn*). The samples at two ranges and at two beam angles are highlighted to show that the volumes associated with these sample ranges and beam angles overlap even within the same ping. This happens because the pulse length and the beam opening angles are larger than the sample distance (sample time) and beam spacing, respectively. (**b**) Side view: Multiple pings along a survey path create samples at regular distance (ping spacing) in the water column (ping nr. *pn*). The covered sample volumes of the last two pings are highlighted to show how samples from consecutive pings additionally overlap depending on the range from the transducer. Vessel motion—which is not depicted in this image—would make the exact volume overlap even more nonuniform.

$$s_V = \frac{\sum\limits_{a \in A_{Sv}} \sigma_{bs;a}}{V} \qquad (12)$$

where,

s_V	Volume backscattering coefficient for the $\left[\frac{m^2}{m^3}\right]$
A_{Sv}	Set of all targets within the sampled volume (V)
V	Sampled volume (m³)

$V_{sn,bn}$ is defined as the volume that would produce the same echo integral as the real acoustic sample, assuming targets are randomly distributed in space (compare "equivalent beam angle" in Simmonds et al. 2005). $V_{sn,bn}$ can be computed as the integral over the entire beam- and range-response functions of each sample (Eqs. 6 and 8):

$$V_{sn,bn} = \int_{R=0}^{\infty} \int_{\theta=0}^{\frac{\pi}{2}} \int_{\varphi=0}^{2\pi} R^2 sin(\varphi) \times BF_{bn}(\theta,\varphi) \times RF_{sn}(R) d\varphi d\theta dR$$
$$(13)$$

where,

$V_{sn,bn}$	Equivalent acoustic sampling volume of sample *sn* of beam b_n

Equation 13 can be solved numerically for arbitrary 3D beam patterns, pulse shapes and different transmit and receive beam steering angles. However, for commonly used mills-cross MBESs, this equation is well approximated by integrating over the transmit and receive beam pattern and the pulse envelope separately (Supporting Information Data S1):

$$V_{sn,bn} \approx R_{sn}^2 \times \Omega_{TX} \times \Omega_{RX;bn} \times c \times \frac{T_{eff}}{2} \qquad (14)$$

$$\Omega_{TX} = \int_{-\frac{\pi}{2}}^{\frac{\pi}{2}} B_{tx0}^2(\vartheta_{y'}) d\vartheta_{y'} \qquad (15)$$

$$\Omega_{RX;bn} = \int_{-\frac{\pi}{2}}^{\frac{\pi}{2}} B_{rx0;bn}^2(\vartheta_{x'}) d\vartheta_{x'} \qquad (16)$$

$$T_{eff} = \int_0^{\infty} p_{env}^2(t) dt \qquad (17)$$

where,

Ω_{TX}	Equivalent one-way beam angle of the main axis transmit beam pattern (rad)
Ω_{RX}	Equivalent one-way beam angle of the main axis receive beam pattern of beam b_n (rad)
T_{eff}	Equivalent pulse duration of the MBES (s)

These approximations allow for a visual understanding of MBESs water column data where each acoustic sample represents the aggregated backscattering cross section of the targets within an equivalent acoustic sample volume (Fig. 3). The

physical constraints of this volume (Fig. 3c) can be described by approximating the beam- and pulse-response functions to equivalent rectangular functions:

$$p_{\mathrm{env}}^2(t) \approx \tilde{p}_{\mathrm{env}}^2(t) = \begin{cases} 1, & -\dfrac{T_{\mathrm{eff}}}{2} \le t \le \dfrac{T_{\mathrm{eff}}}{2} \\ 0, & \mathrm{else} \end{cases} \quad (18)$$

$$B_{tx0}^2(\vartheta_{\gamma'}) \approx \tilde{B}_{tx0}^2(\vartheta_{\gamma'}) = \begin{cases} 1, & -\dfrac{\Omega_{TX}}{2} \le \vartheta_{\gamma'} \le \dfrac{\Omega_{TX}}{2} \\ 0, & \mathrm{else} \end{cases} \quad (19)$$

$$B_{rx0;bn}^2(\vartheta_{x'}) \approx \tilde{B}_{rx0;bn}^2(\vartheta_{x'}) = \begin{cases} 1, & -\dfrac{\Omega_{RX;bn}}{2} \le \vartheta_{bn} - \vartheta_{x'} \le \dfrac{\Omega_{RX;bn}}{2} \\ 0, & \mathrm{else} \end{cases} \quad (20)$$

where,

$\tilde{p}_{env}(t)$	Approximated pulse envelope
$\tilde{B}_{tx0}(\theta)$	Approximated transmit beam pattern
$\tilde{B}_{rx0;bn}(\vartheta)$	Approximated receive beam pattern for beam b_n

Using the spatial domain of the idealized equivalent acoustic sample volumes, Eq. 11 can be simplified and combined with Eqs. 1 and 10 to:

$$\mathrm{EL}_{pn,sn,bn} \approx \mathrm{SL} - 2\mathrm{TL}(R_{sn}) + 10\log\left(\sum_{a \in A_{pn,sn,bn}} \sigma_{bs;a}\right) \quad (21)$$

where,

$A_{pn,sn,bn}$	Set of all bubbles within the spatial domain of the idealized acoustic sample volume described by Eqs. 18–20 (Fig. 3c)
$\mathrm{TL}(R_{sn})$	Transmission loss approximated using the sample's range R_{sn}

Equation 21 can be solved to compute an approximation of the aggregated backscattering cross section and thus of the volume backscattering coefficient (Eq. 12) for each acoustic sample volume:

$$s_{V;pn,sn,bn} \approx \tilde{s}_{V;pn,sn,bn} = 10^{\frac{\mathrm{EL}_{pn,sn,bn} - \mathrm{SL} + 2\mathrm{TL}(R_{sn}) - 10\log\left(V_{sn,bn}\right)}{10}} \quad (22)$$

where,

$\tilde{\sigma}_{AG;pn,sn,bn}$	Estimated aggregated backscattering cross section for sample pn, sn, bn
$s_{V;pn,sn,bn}$	True volume backscattering coefficient for the idealized acoustic sample pn, sn, bn (Fig. 3c)
$\tilde{s}_{V;pn,sn,bn}$	Estimated volume backscattering coefficient for sample pn, sn, bn

Equations 21 and 22 include an approximation error that depends on the exact distribution of the targets in the water column. This error is small for acoustic samples that are located within large clouds (relative to the sample volume) of homogeneously distributed targets. For such a target cloud, it is possible to derive the aggregated backscattering cross-section by multiplying the mean s_V value with the cloud's physical size (e.g., Diner 2007). However, target clouds that are smaller than the acoustic sample volume (e.g., individual bubble streams) are typically underestimated by such an approach (comparable to small fish shoals in Diner 2007).

We are not aware of an existing MBES WCI processing approach that applies well to measuring the aggregated backscattering cross section of gas bubble streams, which are neither segregated small targets, nor large, homogeneously distributed target clouds. We therefore propose a novel inversion approach in the following section.

Echo grid integration for estimating backscattering cross-sections from MBES WCI surveys

Consider a MBES WCI survey that consists of straight survey lines where the vessel is emitting pings at a regular time interval while moving forward. To avoid missing small bubble streams, the ping rate should be chosen such that the acoustic sample volumes of consecutive pings overlap in the water column (Urban et al. 2016). The exact overlap of the acoustic samples varies with range and beam angle and is nonuniformly influenced by vessel's motion (heave, yaw, pitch, and roll) which occurs while moving forward. Thus, each location in the observed water volume is covered by a varying amount of acoustic sample volumes (Fig. 4). Simply integrating backscattering cross-section measurements from these samples would thus lead to an overestimation, since each target is counted by multiple samples.

To prepare these samples for quantitative processing, they are converted to represent $s_{V;pn,sn,bn}$ (Eq. 22) and georeferenced using the ship's navigation and motion data and ray tracing routines (see Urban et al. 2016). The measurements now represent 3D scatter points that are nonuniformly distributed in space.

Now, a high-resolution spatial 3D voxel grid is defined where each grid cell (voxel) represents a cuboid volume that connects to the neighboring voxels without empty space or overlap (Fig. 5). The size of the voxels is adapted to the density of the acoustic samples in the water column (see comments and recommendation section 5.2).

The acoustically measured volume backscattering coefficients are now used to estimate the volume backscattering coefficients for the spatial domain of each voxel cell. For this estimation, we investigated two different averaging methods, which are described below. The comparison of these two gridding methods is presented in the assessment chapter.
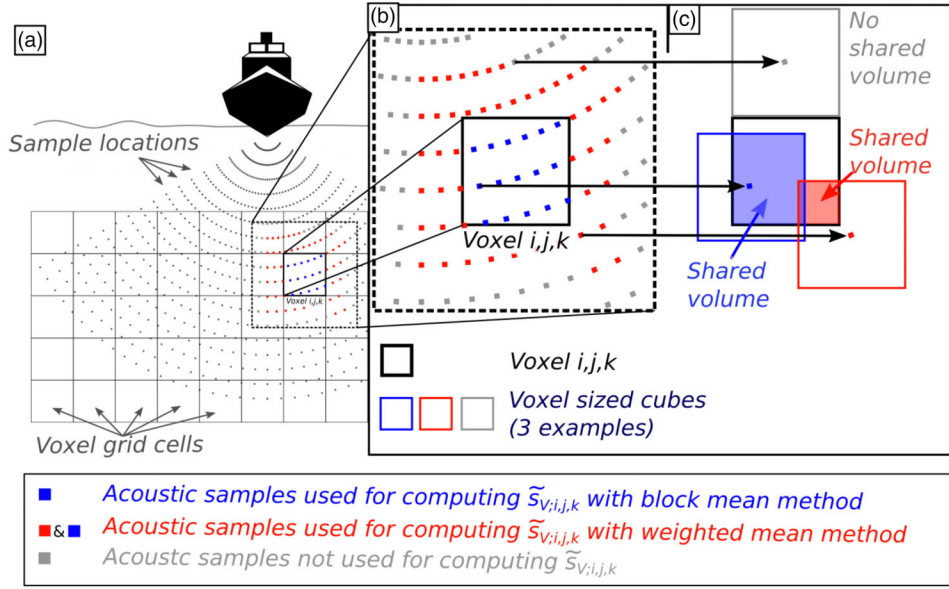
Fig. 5. 2D sketch of the gridding methods at the example of one voxel i, j, k. Method 1 (block mean): The value is computed as average over the acoustic samples within the spatial domain of the voxel (blue samples). Method 2 (weighted mean): A voxel sized cube is placed at the center of each sample (three examples are highlighted in image **c**). The amount of shared volume ($VI_{pn,sn,bn;i,j,k}$) between this cube and the voxel i, j, k is used as weight for a weighted mean overall samples where $VI_{pn,sn,bn;i,j,k} > 0$. Unlike for method 1, each sample may influence up to eight surrounding voxels.

Block mean gridding

The $\tilde{s}_{V;pn,sn,bn}$ value of each acoustic sample is assigned to the voxel i, j, k that contains the sample's center position (Fig. 5). $\tilde{s}_{V;i,j,k}$ is then computed as the mean of all $\tilde{s}_{V;pn,sn,bn}$ values assigned to the respective voxel:

$$\text{Method 1}: \quad \tilde{s}_{V;i,j,k} = \frac{1}{N_{i,j,k}} \sum_{pn,sn,bn \in M_{i,j,k}} \tilde{s}_{V;pn,sn,bn} \quad (23)$$

$$M_{i,j,k} = \left\{ pn, sn, bn \left| \begin{array}{l} \left(x_{i,j,k} - \Delta x/2 < x_{pn,sn,bn} \leq x_{i,j,k} + \Delta x/2\right) and \\ \left(y_{i,j,k} - \Delta y/2 < y_{pn,sn,bn} \leq y_{i,j,k} + \Delta y/2\right) and \\ \left(z_{i,j,k} - \Delta z/2 < z_{pn,sn,bn} \leq z_{i,j,k} + \Delta z/2\right) \end{array} \right. \right\} \quad (24)$$

where,

i, j, k	Three-dimensional index for the grid voxels
$\tilde{s}_{V;i,j,k}$	Estimated volume backscattering coefficient for voxel grid cell i, j, k
$N_{i,j,k}$	Number of acoustic samples, which fall within the spatial domain of the voxel i, j, k
$M_{i,j,k}$	Set of the acoustic sample indices, which belong to the samples which fall within the spatial domain of the voxel i, j, k
$[x, y, z]_{i,j,k}$	x, y, and z position of voxel i, j, k (m)
$[x, y, z]_{pn,sn,bn}$	x, y, and z position of acoustic sample pn, sn, bn (m)
$[\Delta x, \Delta y, \Delta z]$	x, y, and z grid cell size of the voxel grid (voxel dimensions) (m)

$[x, y, z]_{pn,sn,bn}$, x, y, and z position of acoustic sample pn, sn, bn (m);

$[\Delta x, \Delta y, \Delta z]$, x, y, and z grid cell size of the voxel grid (voxel dimensions) (m).

This is the same gridding method used by Urban et al. (2016) to create acoustic flare maps. However, it was not investigated how suitable this approach is for reaching quantitative estimates.

Weighted mean gridding

A virtual cube with the dimensions of a voxel grid cell is placed at each acoustic sample's center position. $\tilde{s}_{V;pn,sn,bn}$ of each sample is then assigned to the eight regular grid cells that volumetrically overlap with this ungridded cube (Fig. 5). The amount of shared volume is used as weight for a weighted mean over the $\tilde{\sigma}_{V_{Vox};pn,sn,bn}$ values associated with each voxel i, j, k:

$$\text{Method 2}: \quad \tilde{s}_{V;i,j,k}$$
$$= \frac{1}{W_{i,j,k}} \sum_{pn,sn,bn \in O_{i,j,k}} \left(\tilde{s}_{V;pn,sn,bn} \times VI_{pn,sn,bn;i,j,k}\right) \quad (25)$$

$$W_{i,j,k} = \sum_{pn,sn,bn \in O_{i,j,k}} VI_{pn,sn,bn;i,j,k} \quad (26)$$

$$VI_{pn,sn,bn;i,j,k} = \frac{\Delta x - \left|x_{i,j,k} - x_{pn,sn,bn}\right|}{\Delta x} \times \frac{\Delta y - \left|y_{i,j,k} - y_{pn,sn,bn}\right|}{\Delta y}$$
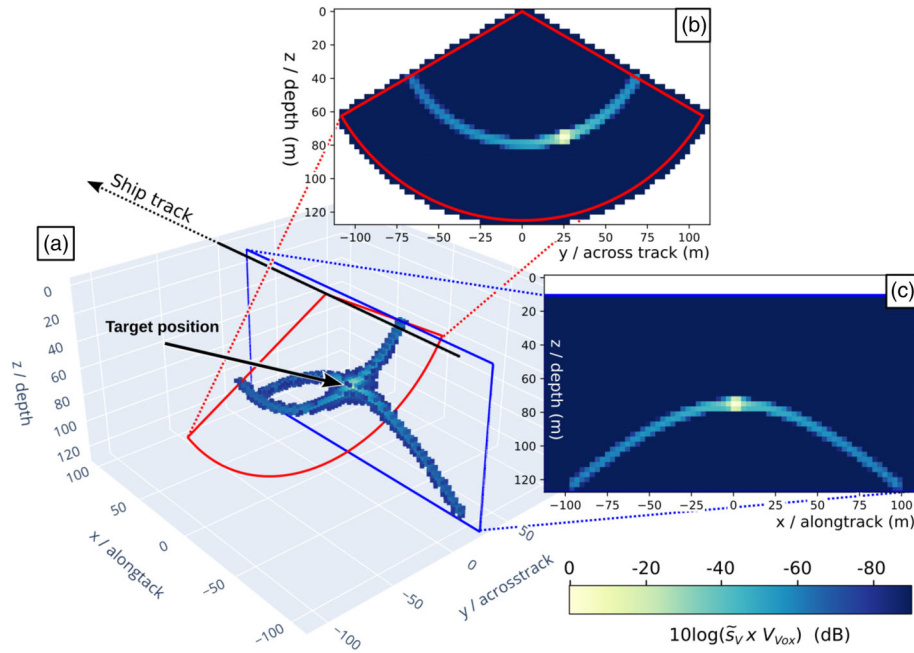$$\times \frac{\Delta z - \left|z_{i,j,k} - z_{pn,sn,bn}\right|}{\Delta z} \quad (27)$$

Fig. 6. Resulting 3D voxel grid for the numerical simulation for a single target at $1x,25y,75z$. The ship moved along the x-axis and created a ping every 0.8 m. Other parameters: Exp. beam pattern, 3 m voxel grid cell size. (**a**) Resulting weighted mean voxel grid (Threshold for visualization: -80 dB); (**b,c**) each represent a one voxel wide slice through the grid at the true target position. The slices show the side-lobe pattern of the receive- (**b**) and transmit- (**c**) beam pattern that are typical for mills-cross MBES WCIs and are the cause for the spreading of the targets influence in the EWC. Reconstructing the true backscattering cross section ($\tilde{\sigma}_{AG;EWC}$) of the target requires summing overall these (influenced) voxel values.

$$O_{i,j,k} = \left\{ pn,sn,bn \left| \begin{array}{l} x_{i,j,k} - \Delta x < x_{pn,sn,bn} < x_{i,j,k} + \Delta x \; and \\ y_{i,j,k} - \Delta y < y_{pn,sn,bn} < y_{i,j,k} + \Delta y \; and \\ z_{i,j,k} - \Delta z < z_{pn,sn,bn} < z_{i,j,k} + \Delta z \end{array} \right. \right\} \quad (28)$$

where,

$VI_{pn,sn,bn;i,j,k}$	Volume intersection between a voxel sized cube at the position of the acoustic sample pn,sn,bn and the voxel i,j,k
$W_{i,j,k}$	Sum overall volume intersections of the samples related to $\{pn,sn,bn \in O_{i,j,k}\}$
$O_{i,j,k}$	Set of the acoustic sample indices pn,sn,bn where a voxel-sized cube with the center position of the acoustic sample shares volume with the voxel i,j,k

The gridded volume backscattering coefficients can be multiplied with the voxel volume to compute estimates of the aggregated backscattering cross section of the targets for each voxel cell. However, the beam pattern and pulse shape of the MBESs cause the acoustic measurements to spread over multiple voxels that did not contain the original targets (Fig. 6). This effect can be compared with smearing the true backscattering cross section of a target over multiple influenced voxel cells. Consequently, we hypothesize that the true backscattering cross section of

the targets in the EWC can be reconstructed by summing up all gridded values that have been influenced by respective targets (Fig. 6):

$$\sigma_{AG;EWC} \approx \tilde{\sigma}_{AG;EWC} = \sum_{i,j,k} \tilde{s}_{V;i,j,k} \times V_{Vox} \quad (29)$$

where,

$\sigma_{AG;EWC}$	True aggregated backscattering cross section of the targets in the EWC
$\tilde{\sigma}_{AG;EWC}$	Estimated aggregated backscattering cross section of the targets in the EWC
V_{Vox}	Volume of a voxel element from the grid

We further hypothesize that for bubble streams of constant flow rate, the aggregated backscattering cross sections of the bubbles within a water column layer BL (Fig. 1) can be reconstructed by summing up only the gridded values that belong to the respective horizontal layer:

$$\sigma_{AG;BL} \approx \tilde{\sigma}_{AG;BL} = \sum_{i,j,k \in K_{BL}} \tilde{s}_{V;i,j,k} \times V_{Vox} \quad (30)$$

where,

$\sigma_{AG;BL}$	True aggregated backscattering cross section of targets within the water column layer BL
$\tilde{\sigma}_{AG;BL}$	Estimated aggregated backscattering cross section of targets within the water column layer BL
K_{BL}	Set of voxel indices i, j, k that belong to the horizontal water column layer BL

Equations 29 and 30 represent what we define as "echo grid integration". This term was chosen to emphasize the similarity and the difference to classic echo integration methods (e.g., MacLennan 1990; Simmonds et al. 2005). For these methods the acoustic measurements are typically integrated/averaged to larger measurements directly. The applied high-resolution spatial gridding of the acoustic measurements produces distinctly different integration results.

In this work, we investigate the validity of Eqs. 29 and 30—and the related approximation errors for different realistic scenarios—empirically by a numerical simulation in the assessment chapter. Note that Eqs. 29 and 30 describe estimates; errors in individual measurements are thus expected. The questions assessed in this work are therefore: Do these errors fall within a reasonable error interval? And: Do they cause statistical biases in repeated measurements? (See results 3.1 for Eq. 29 and 3.5 for Eq. 30).

An invalid estimation method could also introduce measurement biases that depend on survey- or processing parameters (e.g., vessel motion or grid-cell size) or the position of the targets relative to the survey path (depth, range, or beam angle). Such dependencies would make the comparison of measurements from different surveys or different target locations difficult. The assessment will thus specifically investigate if these parameters influence the echo grid integration results (see results 3.2–3.4). Note that this assessment focuses on the effects caused by geometric constraints, sample volumes, beam pattern, pulse envelope, vessel motion, and relative target location. Noise sources that will influence weak targets in a noisy environment are not directly simulated. However, the effect of detection thresholds—that separate the target signals from noise—is discussed in section 3.6.

Assessment

Simulation, settings, and scenarios

A python based numerical simulation of the MBES data acquisition process was created to verify that echo grid integration allows for deriving the aggregated backscattering cross section of targets/bubble streams in the water column. This program is publicly available here: Urban and Peschke (2023). The created simulation computes the WCIs along a virtual survey path for each acoustic sample using Eqs. 1, 10, and 11. The simulated acoustic sample values are converted to $\tilde{s}_{V;pn,sn,bn}$ using Eqs. 22 (assuming complete knowledge of SL

and TL). Subsequently, they are geo-referenced and interpolated onto a regular 3D voxel-grid ($\tilde{s}_{V;i,j,k}$ values) using the previously described echo-gridding approaches. Finally, Eqs. 29 and 30 are applied to the grids respectively to estimate the summed backscattering cross-section of all simulated targets (Eq. 29) or of the target layer (Eq. 30). The different simulation settings used in the simulation are described in the following paragraphs.

To verify Eqs. 29 and 30 two distinct target scenarios were implemented:

1. Single target scenario: A survey over a single static target in the water column with a virtual backscattering cross section = 1 is simulated (Fig. 6). $\tilde{\sigma}_{AG;EWC}$ is estimated by summing all voxel values of the created echo-grid (Eq. 29). This scenario causes worst-case errors for the echo grid integration method. Because of the assumed perfect linearity (Eq. 4), using multiple targets, or target clouds would be equivalent to averaging over multiple single-target measurements and thus lead to a reduction of the echo grid integration error.
2. Bubble stream scenario: A single bubble stream is simulated as a set of static targets, vertically spaced in 10 cm distance in a straight line within a water depth of 1–125 m (Fig. 15). Each individual target was randomly shifted in x, y, and z direction using a Gauss normal distribution with a sigma of 10 cm. In this scenario, $\tilde{\sigma}_{AG;BL}$ is computed for predefined water column layers (BL) by summing up all voxels of the respective layer (Eq. 30). This setting thus allows for investigating biases caused by cutting voxel layers through the water column.

Furthermore, three different vessel motion scenarios were implemented for the simulated data acquisition:

1. Survey path with ideal vessel motion: The ship track is simulated as a straight line where the vessel/MBES moves in x direction over simulated targets and pings at fixed intervals/spacing. The starting position of the track is varied randomly in x, y, and z direction by ± 0.5 the grid cell size for each simulation iteration.
2. Survey path with real vessel motion: Same as the previous scenario, but includes real vessel motion data (roll, pitch, yaw, heave, and ping spacing) from a survey line recorded during Meteor Expedition M143 (Riedel et al. 2018). For each simulation, a different random period within the recorded motion data is chosen to modify the MBES movement. The values varied between $+/-1°$ yaw, $+/-0.2°$ pitch/roll, $+/-70$ cm heave (Fig. 7).
3. Survey path with exaggerated vessel motion: Same as the previous scenario but the vessel pitch, roll and heave motion data have been exaggerated by a factor of 3 to simulate rougher sea conditions. The motion values vary between $+/-1°$ yaw, $+/-0.6°$ pitch/roll $+/-2.10$ m heave.
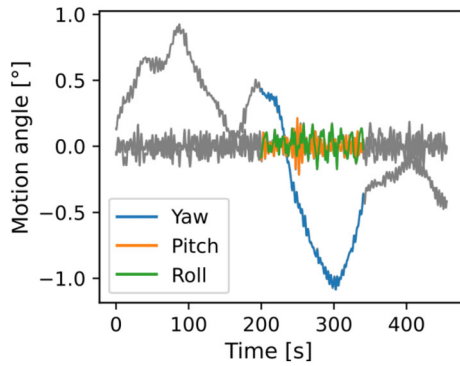
Fig. 7. Recorded yaw/pitch/roll values from a survey track of Meteor M143. Gray depicts the data over the entire survey line. The colored lines mark the data of a random time block chosen for one simulation iteration.

The pulse envelope of the MBES was simulated to be Hann shaded (Fig. 8). For the beam response functions three settings were implemented using scipy.signal.windows (Virtanen et al. 2020) to investigate the effects of different beam patterns (Fig. 9) on the echo grid integration performance:

1. Unshaded beam pattern: The receive- and transmit beam pattern are computed as the response of a steered-line array (128 elements with a spacing of half the wavelength) using Delay-and-Sum beamforming with no shading function applied (Fig. 9). This results in a beam pattern with a narrow main lobe and strong side-lobes (~-13 dB, Fig. 9).

2. Exponentially shaded beam pattern: Same as 1., but an exponential window ($\tau =$ number of transducer elements/2) on the transducer elements. This shading slightly increases the width of the main beam lobe but improves the side-lobe suppression (~-20 dB, Fig. 9).

3. Hann shaded beam pattern: Same as 1., but a Hann window was applied to the transducer elements. This shading results in strong suppression of the side-lobes (~-31 dB) but strongly increases the width of the main lobe (Fig. 9).

Fig. 9. Comparison of receive beam pattern (128 transducer elements) at beam steering angle $0°$. The exponential shading reduces the highest side lobe from -13 to -20 dB but slightly increases the beam width of the main lobe (unshaded: $1.1°$, exponential window: $1.2°$). Hann shading suppresses the first side lobe by an additional 11 dB at the cost of a significant increase of the main lobe beam width. (Hann window: $1.7°$).

The remaining simulated survey settings and MBES parameters (Table 1) represent conditions of a real water column imaging survey that was conducted to detect and quantify gas bubble streams at the shelf of the Black Sea during M143 using a Kongsberg EM710 MBES (Riedel et al. 2018).

Statistical evaluation of the simulation results

All above-mentioned setup options are combined to different simulation scenarios to assess the method performance under varying conditions. The conducted assessment for each scenario can be summarized as:

1. Place the virtual target/bubble stream at a random position in the water column. The location of the targets remains static during this simulated survey.

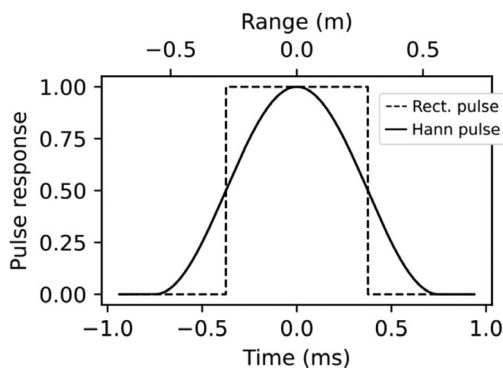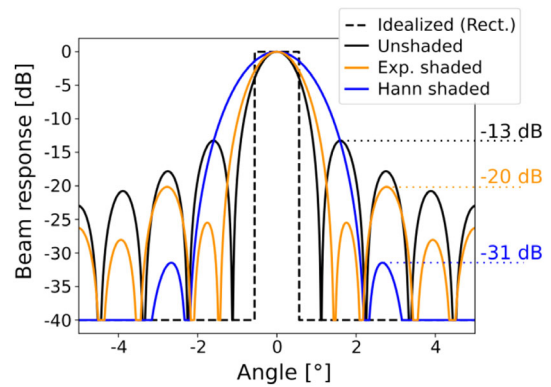2. Simulate an MBES survey over the target/targets and georeferenced the simulated WCIs to 3D scatter points.

Fig. 8. Pulse envelope/range response function for a Hann shaded pulse compared to rectangular pulse of the same effective pulse length (750 μs). The time to range conversion assumes a sound velocity of 1500 m s^{-1}.

Table 1. Simulation parameters, which mimic a survey with a Kongsberg EM710 during Meteor expedition M143.

Simulation parameter	Values
Maximum recording range of MBES (R_{MBES})	125 m
Survey speed	3 knots
Ping interval	2 pings/s $=$ > 0.8 m/ping
Size of the transmit and receive line array	128 elements $=$ > beam width $\sim 1°$x$1°$
MBES beams	256 beams, equiangularly spacing from $-60°$ to $60°$ (α_{Swath}). This results in an equiangular beam spacing of $\sim 0.47°$
MBES sample interval	0.432 ms
Effective pulse duration T_{eff}	0.75 ms

3. Grid the data and estimate the aggregated backscattering cross section using echo grid integration. (Eqs. 29 or 30 depending on the target scenario).
4. Compare the estimated backscattering cross section with the true aggregated backscattering cross section of the simulated target/targets.

For statistical analysis, these steps were repeated ~ 1200 times for each scenario whereas the target, or the bubble stream, was placed at a new random position in the observed water column for each simulation iteration.

The measurement bias (M_{bias}) of the proposed method is quantified for each simulation scenario as the difference between the mean measured aggregated backscattering cross section and the true aggregated backscattering cross section of the simulated targets. The measurement dispersion is described using twice the standard deviation (2SD) and the maximum absolute deviation (MD_{max}) of the measured backscattering cross sections. Thus, $\pm 2SD$ describes a confidence interval containing $\sim 95\%$ of the measurements (assuming a normal distribution) while the interval of $\pm MD_{max}$ contains all simulated measurements and therefore describes the extremes of the error distribution. All statistical parameters in this manuscript are presented in %, relative to the true aggregated backscattering cross section of the simulated targets.

For the assessment, only targets within the acoustically observed water column ($V_{Meas.}$, Fig. 10; Table 2) were considered since targets outside this volume cannot be measured correctly (see also Urban et al. 2016). As shown in results section 3.2, targets that occur close to the boundaries of $V_{Meas.}$ are subject to significant measurement errors when applying echo grid integration. Using the results from section 3.2, we defined the water volume where targets can be correctly measured as $V_{Meas.Opt}$ (Fig. 10; Table 2). Note, that the exact extent of $V_{Meas.Opt}$ may vary with survey and system parameters (see section 3.2).

Table 2. Extends of $V_{Meas.Opt}$ where the measurements of targets were found to be free of boundary effects for the simulated scenarios (Fig. 10; see results section 3)

$V_{Meas.}$ and $V_{Meas.Opt}$ variables	Values
Maximum recording range of MBES (R_{MBES})	125 m
Limited minimum range ($R_{Lim;Min}$)	45 m
Limited maximum range ($R_{Lim;Max}$)	120 m
Swath opening angle of MBES (α_{Swath})	$\pm 60°$
Limited across-track angle from the survey path ($\alpha_{Lim;Max}$)	$\pm 50°$
Along track extend of $V_{Meas.}$ and $V_{Meas.Opt}$ (D_x)	$+/-0.5$ of the voxel size of the used grid

Results

Validation and comparison of the two gridding methods

For initial validation of the proposed method, the single target scenario with the ideal vessel motion setting and a 3 m voxel size was used. The simulation was conducted for each beam pattern setting and $\tilde{\sigma}_{AG;EWC}$ was computed using both proposed voxel gridding methods. As described in the previous section, the simulation results were filtered to only include measurements for targets from within $V_{Meas.Opt}$ (Table 2; Fig. 11b); this filtering resulted in ~ 800 accepted measurements per simulation (Supporting Information Table S2).

M_{bias} for both gridding methods and all simulated scenarios was $<\pm 0.7\%$ (Supporting Information Table S2). This low measurement bias validates Eq. 29 and shows that echo grid integration can be used for estimating the true backscattering cross section of targets within $V_{Meas.Opt}$.

However, the measurement dispersion for block mean gridding was significantly higher compared to weighted mean gridding. For the exponentially shaded beam pattern (Fig. 11), MD_{max} was only $\sim 2.6\%$ for the weighted mean method
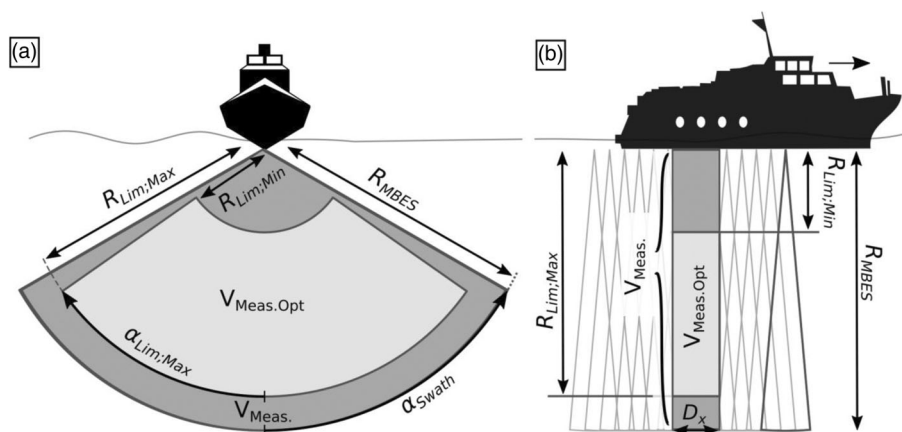

Fig. 10. Water volume where a virtual target was randomly placed for each simulation iteration ($V_{Meas.}$) and the limited volume where targets were found to be optimally measured by the survey ($V_{Meas.Opt}$, see results section 3). (**a**) Front view. (**b**) Side view.
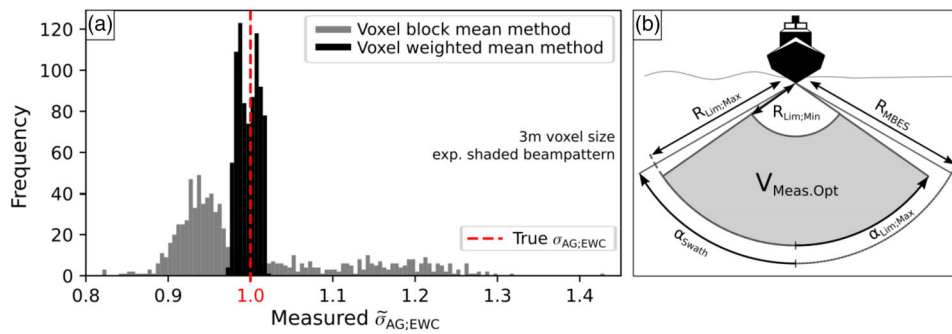
Fig. 11. (**a**) Histogram of the measured $\tilde{\sigma}_{AG;EWC}$ for ~ 800 simulations using the exponentially shaded beam pattern. The red line marks the true back-scattering cross section of the simulated target. The measurements using weighted mean gridding have a significantly lower measurement dispersion compared to block mean gridding. (**b**) The water volume where targets may occur was limited to $V_{Meas.Opt.}$ to avoid boundary effects for this evaluation.

compared to a MD_{max} of $\sim 43\%$ for block mean method. Similar differences between the gridding methods were found for the other tested beam pattern scenarios (Supporting Information Table S2). Because of this significant outperformance of weighted mean gridding over block mean gridding, the mean gridding—which was used in Urban et al. (2016)—is not further considered in this work.

Influence of the relative target position

The density of the acoustic samples, their volume and overlap vary strongly throughout the water column (Fig. 4). In this section, we evaluate if these conditions influence the quantification results for targets in different regions of the EWC. For this, we used the same simulation scenario described in the previous section. However—to investigate the boundary effects—also the results from targets outside $V_{Meas.Opt}$ were considered. The Hann shaded (strong side-lobe suppression and wide main lobe) and the unshaded (weak side-lobe suppression and narrow main lobe) beam pattern settings are used in this comparison.

Influence of target across-track angle

To investigate the influence of the target across-track angle, the volume in which targets may occur was limited by the range limits $R_{Lim;Min}$ and $R_{Lim;Max}$ (Table 2) but not by limiting

the swath angle ($V_{Meas.FullAngle}$, Fig. 12b). Results were sorted by the target across-track angle and—to better highlight trends—smoothed using a $2°$ wide block mean filter along the across-track angle axis (Fig. 12a).

For the Hann shaded beam pattern setting, the measured $\tilde{\sigma}_{AG;EWC}$ were stable with a low measurement bias ($\sim -0.1\%$) for targets along the across-track angular axis except for the outer parts of the swath ($> 50°$; Fig. 12a). For the unshaded beam pattern setting, a small measurement bias ($\sim -0.5\%$) was observed for targets between $0°$ and $\sim 35°$; this increased to $\sim -1\%$ for larger target across-track angles (Fig. 12a). The strong measurement deviation at the outer parts of the swath ($> 50°$) is likely caused by incompletely covered voxels at the outer swath boundary.

Influence of target range

To investigate the influence of the target range, the considered volume where targets may occur is restricted by limiting the across-track angle to $\alpha_{Lim;Max}$ (Table 2) but not the range ($V_{Lim;FullRange}$, Fig. 13b). The measured $\tilde{\sigma}_{AG;EWC}$ values are then sorted by the target range (Fig. 13a).

Results for the measurement performance were stable between a beam pattern dependent upper range limit (27 m for Hann shaded beam pattern and 41 m for the unshaded
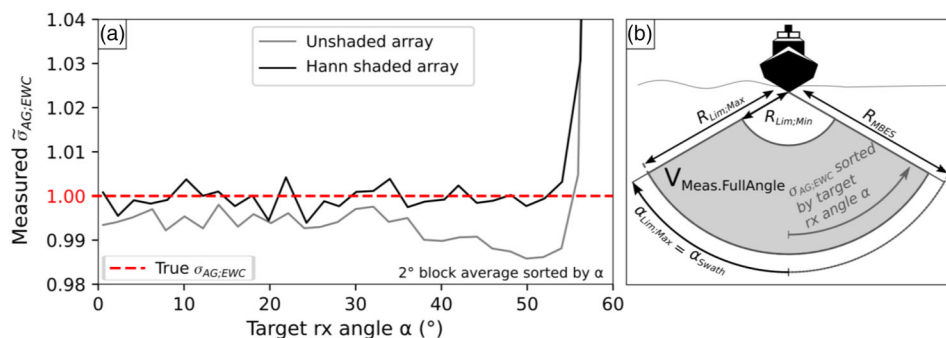

Fig. 12. Angular dependency of $\tilde{\sigma}_{AG;EWC}$ for unshaded and Hann shaded beam pattern (3 m grid, weighted mean gridding). The red line marks the true backscattering cross section of the simulated target. The results are sorted by the target receive angle and averaged over $2°$ blocks to highlight angular dependent trends. Nearly, no influence of the across-track angle can be seen except for targets at the outer extend of the swath ($> 50°$).
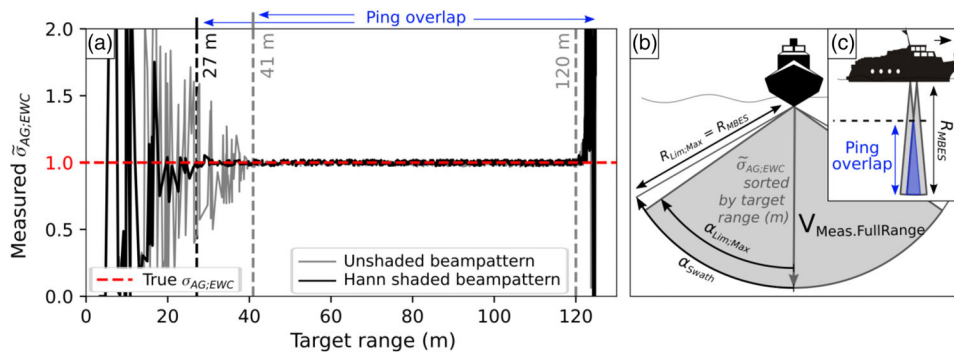
Fig. 13. (**a**) $\tilde{\sigma}_{AG;EWC}$ measured by weighted voxel averaging method for unshaded and Hann shaded beam pattern scenario (ideal motion; 3 m voxel size). The red line marks the true backscattering cross section of the simulated target. The measured values were sorted by the range of the simulated target; 27 m and 41 mark the range where pings overlap for the Hann shaded/unshaded beam, respectively (**c**). (**b**) The water volume where targets may occur was extended to the full range ($V_{Meas.FullRange}$) but limited by the maximum across-track angle. (**c**) Ping overlap range is reached where two consecutive pings overlap. It depends on the vessel speed, ping rate, and transmit beam width.

beam pattern) and a deeper range limit (120 m for both beam pattern settings, Fig. 13a). The larger errors for targets at close range can be explained as an incomplete coverage of the water column where the MBES pings do not overlap (Fig. 13c). The ping overlap depth (Eqs. 31–33) was determined by the ping spacing (here 0.8 m) and the beam width. It was reached at 41 m for the unshaded beam pattern (beam width 1.12°) and 27 m for the Hann shaded beam pattern (beam width 1.69°). These computed ranges fit well with the simulation results (Fig. 13a). The larger echo grid integration errors for ranges > 120 m are again attributed to incompletely covered voxels at the outer swath boundary.

In conclusion, the range and beam angle of measured targets have nearly no effect on the measurement performance; except for targets found at the outer extends of the swath. The limits found of these investigations were used to define the angular range and the sample range where targets can be optimally measured for the simulated MBES survey ($V_{Meas.Opt}$, Table 2). Note that still all beams and all acoustic samples of

the MBES swath must be used for computing the voxel grids, because excluding MBES samples would decrease $V_{Meas.Opt}$.

Influence of real vessel motion and chosen voxel size

The performance of the proposed processing method was evaluated under more realistic conditions by introducing vessel motion. For this, the single target scenario (restricted to $V_{Meas.Opt}$) was simulated for all vessel motion and all beam pattern settings. The data were gridded using the weighted mean method for three different voxel sizes (1, 1.5, and 3 m). The complete results can be found in the Supporting Information Table S3.

M_{bias} was found to be largely independent of the vessel motion and the chosen voxel size (<< 1% for all simulated scenarios and settings, Supporting Information Table S3).

The measurement dispersion was found to be dependent on the simulated vessel motion and the chosen voxel size. This is shown here for the example of the exponentially shaded beam pattern setting in Fig. 14; Table 3. For the ideal
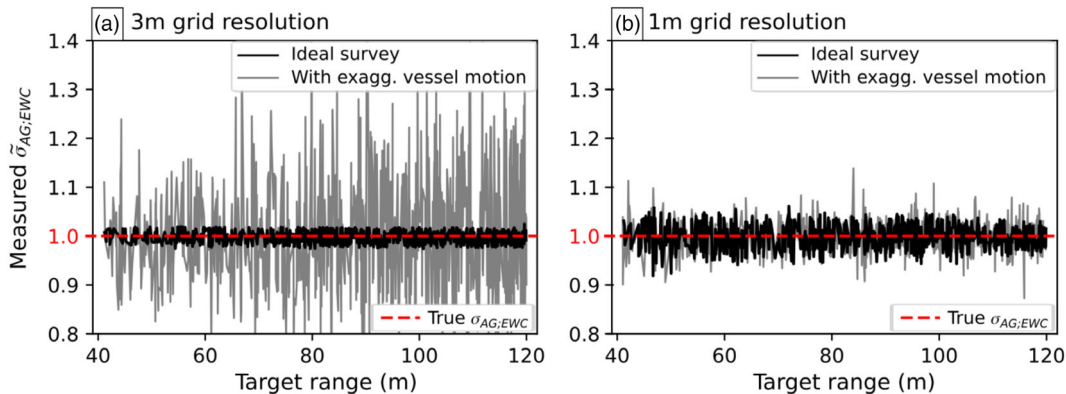

Fig. 14. $\tilde{\sigma}_{AG;EWC}$ measured for the ideal vessel motion and the exaggerated vessel motion setting (single target within $V_{Meas.Opt}$, weighted mean gridding). (**a**) Results for the 3 m grid cell resolution indicate a low measurement dispersion for the ideal vessel motion scenario that significantly increases if vessel motion alters the survey path. (**b**) Results for a 1 m grid cell resolution. Compared to the 3 m voxel size, the measurement dispersion is higher for the ideal vessel motion scenario but remains stable even for the exaggerated vessel motion scenario.

Table 3. Measurement dispersion for the exponential beam pattern setting and a single target for different voxel sizes and vessel motion scenarios (lowest measurement dispersion per motion setting is highlighted bold).

Vessel motion setting	Measurement dispersion property	Voxel size		
		1 m	1.5 m	3 m
Ideal vessel motion	MD_{max} (%)	± 8.1	± 3.6	± **2.6**
	2SD (%)	± 4.9	± 2.6	± **2.5**
Real vessel motion	MD_{max} (%)	± **7.5**	± 10.2	± 16.2
	2SD (%)	± **4.8**	± 4.8	± 9.2
Exaggerated vessel motion	MD_{max} (%)	± **13.8**	± 22.0	± 74.8
	2SD (%)	± **6.2**	± 9.9	± 24.3

vessel motion scenario, smaller voxel sizes showed an increased measurement dispersion compared to larger voxel sizes. However, when introducing real vessel motion, the measurement dispersion increased significantly for the larger voxel sizes but remained relatively stable for the 1 m grid cell resolution (Fig. 14; Table 3). The measurement dispersion increased slightly with the target range for the 3 m and the 1.5 m voxel size settings. This range dependency was not observed for the 1 m grid-cell resolution. Note that the 1 m voxel size is remarkably similar to the spacing between consecutive pings (0.8 m). These findings are used for a discussion on the optimum voxel size in practical applications in comments and recommendation section 5.2.

Influence of different beam pattern

The beam pattern setting—and more specifically the suppression of side-lobe levels—was found to be the determining factor for M_{bias} for all simulated scenarios (Supporting Information Table S3). The unshaded beam pattern, which features the highest side-lobe levels (Fig. 9), thereby caused the highest ($\sim -0.6\%$ for all scenarios) and the Hann shaded beam pattern, with the strongest side lobe suppression, the lowest measurement bias (± 0.1% for all scenarios).

The influence of the beam pattern setting on the measurement dispersion was compared for the 1 m grid-cell resolution. The Hann shaded beam pattern and the unshaded beam pattern settings showed the lowest and highest measurement

dispersions, respectively (Table 4). We attributed this to signal smoothing caused by the size of the main lobe (largest for the Hann shading, smallest for no shading, see Fig. 9). The performance difference between different beam pattern settings was more pronounced when realistic vessel motion was considered in the simulation (Table 4).

Measurement performance for bubble streams

In this section, the measurement performance is investigated for estimating $\tilde{\sigma}_{AG;BL}$ (Eq. 30) of water column layers that cut through simulated bubble streams (Fig. 15). The bubble stream scenario was simulated for all vessel motion and all beam pattern settings and the data were gridded using the weighted mean method and a 1 m voxel size. $\tilde{\sigma}_{AG;BL}$ was inspected for three different water column layers with a central water depth of 42, 60, and 108 m. The vertical thickness of the layer was always 12 m (Fig. 16).

The simulation results were first investigated for positional dependencies of the bubble stream by sorting the results by the across-track position (y) of the simulated bubble stream (Fig. 16). As for the single target scenario, no positional dependency was found except for y-positions that were not covered by the respective layer (Fig. 16). The y-positions where these boundary effects occurred depended on the depth and size of the respective water column layer (Fig. 16b).

For investigating the measurement performance, we only used measurements of bubble streams within a limited y-

Table 4. Measurement dispersion for a 1 m voxel size and a single target, for different beam pattern and vessel motion settings (lowest measurement dispersion per motion setting is highlighted bold).

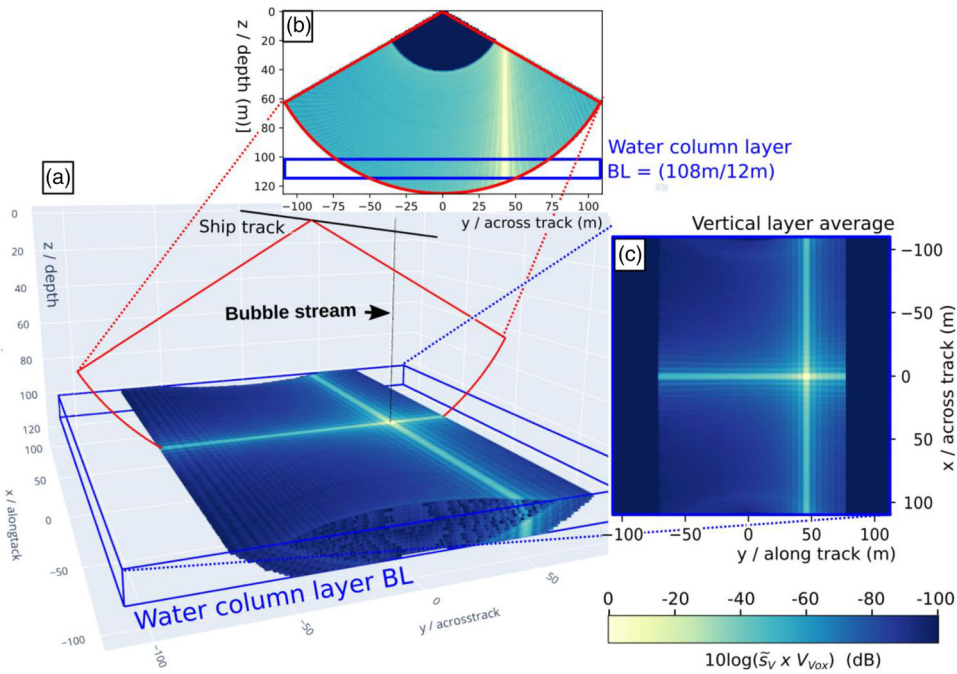| Vessel motion setting	Measurement dispersion property	No beam shading	Exp. beam shading	Hann beam shading
Ideal vessel motion	MD_{max} (%)	± 8.5	± 8.1	± **4.9**
	2SD (%)	± 4.9	± 4.9	± **3.6**
Real vessel motion	MD_{max} (%)	± 14.7	± 7.5	± **6.8**
	2SD(%)	± 5.1	± 4.8	± **3.9**
Exaggerated vessel motion	MD_{max} (%)	± 24.6	± 13.8	± **12.2**
	2SD (%)	± 7.3	± 6.2	± **4.6**

Fig. 15. (a): 3D water column layer (BL) at 108 m water depth that cuts through a bubble stream as simulated for an MBES with exponentially shaded beam pattern (1 m voxel; weighted mean gridding). **(b)** Voxel-sized vertical *x/y* layer cut through the simulation at the bubble stream × position. **(c)** Vertically averaged view of a horizontal water column layer.

position range (± 49 m) where all three water column layers were completely covered by the simulated surveys (Fig. 16). The results can be found in Supporting Information Table S4.

M_{bias} for estimating $\tilde{\sigma}_{AG;BL}$ of water column layers was found to be similar to M_{bias} of the single target setting ($\sim -0.6\%$ for unshaded beam pattern, $\sim -0.2\%$ for exp. shaded and ~ -0.1 for Hann shaded beam pattern). This low bias validates Eq. 30 and shows that the proposed method can estimate the aggregated backscattering cross sections of targets from bubble streams within horizontal water column layers.

The measurement dispersion for the bubble stream scenario was reduced compared to the single target setting (compare Table 5 with Table 4). This was expected since, in the created simulation, the sum over multiple targets reduces the overall error in the same way as averaging over multiple measurements does. Note that in reality, the linear integration of multiple received echo levels (Eq. 4) would include a random statistical uncertainty (e.g., Gorska and Chu 2005; Simmonds et al. 2005) that was not considered here.

A comparison of the three water column layers shows that the measurement dispersion can, by a small degree, vary with depth (Supporting Information Table S4). The exact
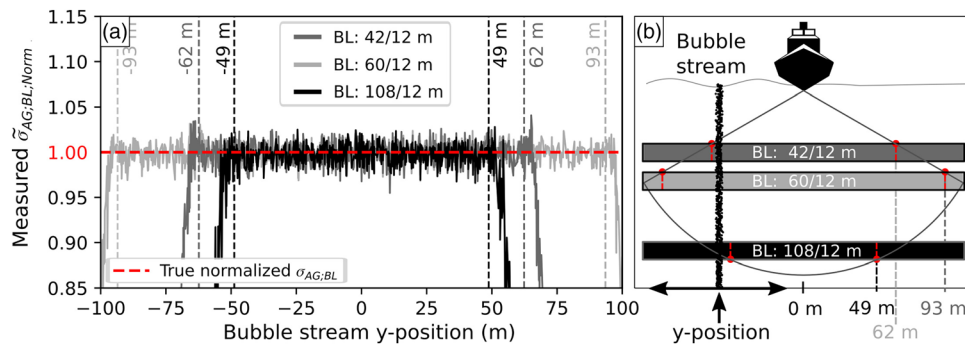

Fig. 16. (a) Simulation results for the bubble stream scenario using three 12 m water column layers (1 m voxel size, exponential beam pattern, and real vessel motion). The $\tilde{\sigma}_{AG;BL}$ values have been normalized by the true backscattering cross section of the bubbles within the respective layer bubble stream layer. The measurements have been sorted by the *y*-position (across-track) of the simulated bubble stream. **(b)** View of the size and position of the three water column layers. The red marks show the *y*-positions where the water column layers intersect with the multibeam swath. For bubble streams outside of these *y*-positions the measurement dispersion strongly increases.

Table 5. Measurement dispersion (maximum dispersion MD_{max} and twice the standard deviation 2SD) for the "bubble stream" setting at t"ree water col"mn layers (12 m vertical layer size, 1 m voxel size, exp. beam pattern, real vessel motion; lowest measurement dispersion of each water column layer is highlighted bold).

Water column layer	Measurement dispersion property	No beam shading	Exp. beam shading	Hann beam shading
42 m depth	MD_{max} (%)	± 3.9	± 4.5	**± 2.9**
	2SD (%)	± 2.2	± 2.4	**± 2.0**
60 m depth	MD_{max} (%)	± 3.0	± 3.2	**± 3.0**
	2SD (%)	± 2.1	± 2.1	**± 1.9**
108 m depth	MD_{max} (%)	± 4.0	± 3.4	**± 3.4**
	2SD (%)	± 2.0	± 2.0	**± 1.7**

relationship seems to depend on the strength of the vessel motion. For the ideal vessel motion scenario, the measurement dispersion decreases with increasing layer depth; conversely, it increases with layer depth for the exaggerated vessel motion scenario (Supporting Information Table S4). For the real vessel motion scenario, an increase in layer depth lowered the standard deviation but increased the maximum measurement dispersion (Table 5).

Like the single target scenario, the Hann beam pattern setting caused the lowest measurement dispersion for all simulated scenarios (Table 5).

Influence of detection thresholds

In practical application, an intensity threshold must be applied to the acoustic data to separate signals of targets from the background noise level. Applying such a threshold to the gridded data leads to excluding voxels from the measurements (Fig. 17) and can thus lead to underestimating the aggregated backscattering cross section of targets in the water column using the proposed echo grid integration method.
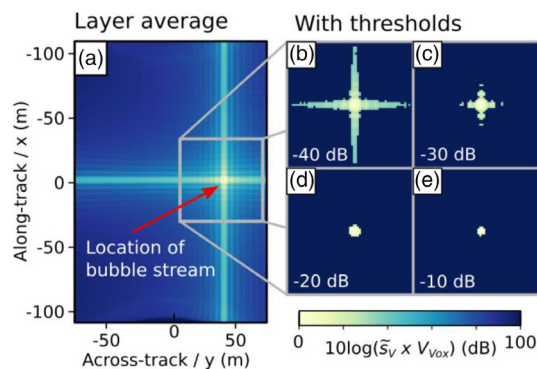
The impact of such a threshold depends on the strength of the acoustic signal returned from the targets in the water column; less voxels are cut by a fixed threshold for strong targets compared to weaker targets, which are visible just above the background noise level. To get an understanding on how high the underestimation caused by a threshold can be, we investigated the measurement bias for the example of measuring a bubble stream after thresholding the results of the 108 m water column layer (Fig. 18 and Supporting Information Table S1). The threshold is given relative to the highest $\tilde{s}_{V;pn,sn,bn}$ value within the layer to make it representative to the backscattering strength of the bubble stream. The results are compared for the different beam pattern scenarios. For the unshaded beam pattern setting, a threshold of −20 dB leads to an underestimation of nearly 10%, while the same threshold only caused 1% underestimation for the Hann shaded beam pattern. This is likely caused by the higher side-lobe levels for
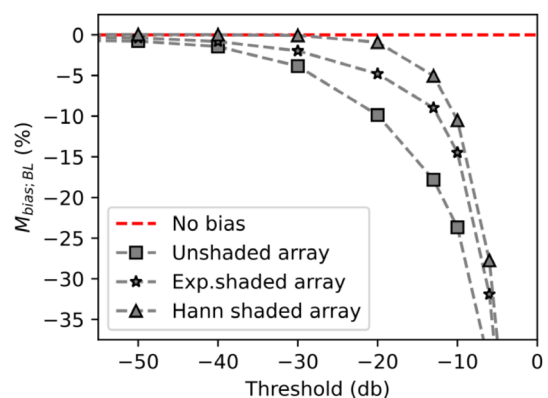

Fig. 18. $M_{bias;BL}$ values computed from ∼ 600 simulations for each beam pattern setting, after applying a threshold to the grids. Threshold dB is relative to maximum $\tilde{s}_{V;pn,sn,bn}$ value within the layer. A high threshold means that more grid cells are excluded from the computation, such that the result is underestimated. The results for shaded beam pattern are more robust against this underestimation. Even at a threshold level of −20 dB, the underestimation is still <1% for the Hann-shaded and <5% for Exp. shaded beam pattern. Processing parameters: 108 m depth, 12 m layer, and 1 m voxel size.

Fig. 17. (**a**) Vertical average of a 12 m water column layer that cuts through a bubble stream at 108 m water depth (exp. shaded beam pattern and 1 m voxel size). (**b**–**e**) Zoom with applied thresholds; underestimation caused by the thresholds is: $B = −0.8\%$, $C = −2.0\%$, $D = −4.8\%$, $E = −14.5\%$.

the unshaded beam pattern which causes a stronger dispersion acoustic energy over multiple voxels.

Summary and discussion

In this work, we presented and investigated a novel method (echo grid integration) to estimate the aggregated backscattering strength of ensonified targets. Echo grid integration can be summarized in the following steps:

1. The multibeam water column data is converted to volume backscattering coefficients and geo-referenced to represent spatial measurement points in 3D space.
2. The volume backscattering coefficients are averaged onto a 3D, high resolution voxel grid. (Two valid gridding methods are described.)
3. Each gridded value is multiplied with the voxel volume to obtain a measurement for the aggregated backscattering cross section within each voxel cell. These individual estimates are erroneous due to signal smearing caused by the acoustic beam pattern and pulse envelope (sample overlap).
4. The aggregated backscattering cross section of the targets that caused this signal is estimated as the integral overall voxel cells affected by the spread signal (see also comments and recommendations 5.3).

Gridding acoustic data have been applied many times for different reasons before (e.g., Urban et al. 2016; Ordoñez et al. 2022). The essence of the echo grid integration method is the application of Eqs. 29 or 30 (step 4) to estimate the summed backscattering cross-section of the targets in the water column. Note that these equations where specifically investigated for multibeam surveys that cover the measured target cloud completely with overlapping pings and overlapping beams and overlapping samples. Echo grid integration is thus a method specifically developed for multibeam systems and is (at least in the presented form) not directly applicable to surveys using single beam echosounder systems.

The validity of the echo grid integration method was assessed using a numerical simulation of MBES data acquisition surveys over targets of known backscattering cross-section. For simplification, we ignored nonlinear acoustic effects, noise, and unwanted targets, assumed spherical bubbles that scatter independent of the acoustic incidence angle and ignored the influence of noise. However, even for such idealized circumstances, measuring individual targets and/or small target clouds (bubble streams) causes significant measurement errors for existing measurement approaches from fishery science. As an example, Diner (2007) reported a measurement bias of more than -3 dB (-50%) for fish shoals smaller than $\sim 1.3\times$ the beam width for a SBES based measurement method that was investigated using a similar simulation assessment as conducted here.

In comparison, the related errors found for MBES echo grid integration can be considered significantly low. Our simulation results show that echo-grid integrals reproduce (with a small approximation error) the total backscattering cross section of individual targets and of target clouds of all sizes (e.g., bubble stream sections) if these targets are sufficiently covered by the acoustic survey. The measurement bias was found to be < 1% if the returned acoustic signal is well detectable above the background noise level. The measurement dispersion was < 5% of the true total backscattering cross section for the simulated scenarios, which mimicked the conditions of a real water column survey (Table 5).

The found echo grid integration error was largely independent of the target/bubble stream position relative to the ships track except for targets occurring close to the outer extends of the ensonified water volume. The upper range limit where these boundary effects occur coincided with ping overlap depth, which is a function of the transmit beam width, the ping rate, and the vessel speed (see comments and recommendations section 5.1). Surveyors should thus make sure that the water column is covered by overlapping pings in the water depth where targets/bubble streams are to be investigated. If the ping rate is reduced due to ping synchronization with other systems, it might be necessary to reduce the survey speed.

The simulation results indicated a lower measurement bias and measurement dispersion for beam pattern with a larger beam width and a stronger suppression of side-lobes. This demonstrates that for water column applications, the highest acoustic resolution may not always give the best results. However, in practical application also the influence of the acoustic resolution and the signal-to-noise ratio must be considered. Especially for deep water applications, a narrow beam width may be key to detect and distinguish bubble streams from, for example, noise, reverberation, or acoustic artifacts.

The comparison of different gridding methods revealed great differences in measurement dispersion. Weighted mean gridding caused a significantly lower measurement dispersion compared to a simple block mean. It is unfortunate that the exact performance of this method is affected by the chosen voxel size, which can be difficult to determine (see comments and recommendations section 5.2). Finding a gridding method, which performs more independent of this processing parameter could thus be an interesting future improvement of this method.

While the effect of noise was not directly simulated in this assessment, we investigated influence of detection thresholds that are necessary to distinguish target clouds from the background noise. (see comments and recommendations section 5.3). As expected, these thresholds cause a measurement bias that depends on how much the measurements exceed the threshold level. However, the strength of this was found to be beam pattern dependent. Using beam pattern with a strong side-lobe, reduces the negative effect of the detection threshold compared to measurements using unshaded arrays.

In conclusion, echo grid integration is suitable for investigating the aggregated backscattering cross section of bubble streams. Using this method, it is possible to use MBESs within existing gas flow quantification methods that have so far been

applied to SBESs (comments and recommendations section 5.4 and 5.5). This may help to avoid the often large and difficult-to-quantify uncertainties related to the limited spatial coverage of SBES surveys (e.g., discussion in Padilla et al. 2019).

When interpreting the described echo grid integration error, it is important to note that the investigated uncertainties relate only to investigating aggregated backscattering cross sections assuming idealized conditions (no ambient noise, no nonlinear acoustic effects, perfectly calibrated system, static target clouds, and isotropic backscattering). Thus, they are only part of a larger error chain when applying the method for quantitative applications. Errors related to acoustic inversion can thereby be high in practical application. Further uncertainties can be caused by unwanted targets or acoustic artifacts (e.g., from seafloor induced side-lobes), which were not considered here. For a brief discussion on detecting and distinguishing bubble stream targets, see comments and recommendations section 5.3. A brief discussion on using uncalibrated MBESs can be found in comments and recommendations section 5.5.

Future studies may aim to reproduce the results presented here, to include more effects for an even more realistic simulation assessment of the expected error, or may aim at assessing the echo grid integration error for a different survey scenario (e.g., different MBES parameters, different vessel motion, and/or a different water depth). Such studies can build on the simulation presented here, which is available as an open-source python program at (link to be included in final version) with example scripts that show how to perform a simulation.

Comments and recommendations

On computing the ping overlap depth

The smallest depth (D_{overlap}; Fig. 19) where the water column is covered by the overlap of consecutive pings can be estimated from the along track beam width using the following equations:
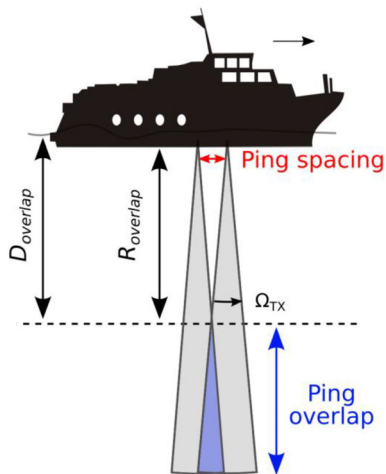

Fig. 19. Variables relevant for computing the depth where consecutive pings overlap ($D_{\text{overlap.}}$)

$$D_{\text{overlap}} \approx R_{\text{overlap}} + Z_{\text{transducer}} \tag{31}$$

$$R_{\text{overlap}} \approx \frac{PingSpacing}{2 \times \tan\left(\frac{\Omega_{TX}}{2}\right)} \tag{32}$$

$$PingSpacing = \frac{VesselSpeed}{PingRate} \tag{33}$$

where,

D_{overlap}	Depth at which the pings overlap (m)
R_{overlap}	Range from transducer at which the pings overlap (m)
$Z_{\text{transducer}}$	Depth of the transducer (m)
$PingSpacing$	Distance between two consecutive pings (m)
Ω_{TX}	Transmit/along track beam width
$VesselSpeed$	Survey speed of the vessel (m s^{-1})
$PingRate$	Ping rate at the survey depth (s^{-1})

These equations show that D_{overlap} can be elevated either by increasing the transmit beam width (if possible), by increasing the ping rate or reducing the survey speed. Note, that very strong vessel movements can cause pings to sporadically overlap at a higher or a lower range than estimated here.

On finding the optimal voxel size

For weighted mean gridding, optimizing the voxel size can reduce the measurement dispersion. It should be noted that, since the voxel size does not influence the measurement bias, the overall estimates of gas flow from areas with hundreds of bubble streams are less influenced by this parameter.

Our findings on the optimal voxel size are summarized as follows: If the vessel moves in a perfectly straight line, a larger voxel size could decrease measurement dispersion. However, of the three voxel sizes tested, the smallest (1 m) caused the lowest measurement dispersion for the scenarios with realistic vessel motion (yaw, pitch, and roll). The 1 m voxel size was thereby remarkably close to the largest void space between acoustic samples; here, this space was determined by the ping spacing of 0.8 m. We therefore recommend adapting the voxel size to roughly match the ping spacing. Users may then use the python simulation to assess the expected measurement dispersion for their specific case and, if necessary, investigate if a larger or smaller voxel size can improve the results.

On distinguishing target blobs and the definition of "target affected" voxels

Equations 29 and 30 describe the sum overall voxels in the investigated water volume. Using these equations, determining the aggregated backscattering cross section of, for example, individual targets, fish-shoals, and bubble streams would not be possible if any other targets are present within the gridded water column data. However, since most of the energy of the beam- and pulse-response functions is concentrated in

a very narrow region of the beam, it is enough to include the voxels that are "significantly affected" by a target (see also results section 3).

These 'target affected voxels are connected (e.g., Figs. 6, 15) and can be detected by applying a threshold followed by a region growing algorithm on each local maxima in the voxel grid. The influences of multiple targets cannot be separated. Thus, if two targets influence the same voxel, the regions connect to one region. The integral over this region is still representative to the aggregated backscattering cross section of all "connected" targets. This simple algorithm does not distinguish between noise, artifacts and target type (e.g., fish or bubbles), which must be achieved by a different method (e.g., Urban et al. 2016 for bubble streams).

On computing gas flow from processed grids

In this section, we discuss a simple example that shows how an existing quantification method (for SBESs) can be applied to the grids created here. Following the approach of Veloso et al. (2015), the volumetric gas flow rate of a bubble stream can be computed from the aggregated backscattering cross section within a water column layer of a defined size (Fig. 1) by:

$$\dot{V} = \tilde{\sigma}_{\mathrm{AG;BL}} \times \frac{\Psi}{D} \tag{34}$$

$$\Psi = \frac{4}{3}\pi \frac{\displaystyle\int_0^\infty r^3 f(r) U(r)\,dr}{\displaystyle\int_0^\infty f(r)\sigma_{bs}(r)\,dr} \tag{35}$$

where,

$\dot{V}$	Volumetric gas flow rate (m^3 s^{-1})
D	Vertical size of the depth layer (m)
Ψ	Flow rate conversion factor (note: compared to Veloso et al. 2015, D has been separated from this factor and put into Eq. 34)
r	Bubble radius (m)
$f(r)$	Probability density function of the bubble-size distribution (m^{-1})
$U(r)$	Bubble rising speed as function of the bubble radius (m s^{-1})
$\sigma_{bs}(r)$	Backscattering coefficient as function of the bubble radius according to the used bubble model. (e.g., Anderson 1950; Thuraisingham 1997; Ainslie and Leighton 2011; Li et al. 2020) (m²)

Using these equations, two approaches can be used to compute the volumetric gas flow rate within MBES WCI data processed with the presented method.

Model inversion approach

The factors $U(r)$ and $\sigma_{bs}(r)$ are gained from bubble models. The most challenging factor is the bubble radii distribution of the measured bubble streams $f(r)$. A typical assumption is that bubble streams in an area have a similar bubble size distribution such that only the distribution of a single bubble stream needs to be measured. This can be done, for example, using direct camera observations at the release spot at the seafloor. The bubble size distribution for the depth of the acoustically investigated water column layer can be predicted from this initial data using a bubble dissolution model (e.g., McGinnis et al. 2006; Rehder et al. 2009; Jansson et al. 2019). The found Ψ factor (Eq. 35) can then be applied to all bubble streams in the area.

Direct calibration approach

If the bubble size distribution $f(r)$, and therefore the factor Ψ, can be assumed to be constant for all gas bubble streams in the area, the relationship between $\tilde{\sigma}_{\mathrm{AG;BL}}$ and $\dot{V}$ can be expected to be approximately linear. Determining $\tilde{\sigma}_{\mathrm{AG;BL}}$ for a single bubble stream of known flow rate would thus be enough for to determine Ψ and thus to directly calibrate the voxel grid for gas flow rate assessments.

It should be noted that these approaches assume perfectly spherical bubbles. Larger gas bubbles may also take an ellipsoidal (nonspherical) shape such that their exact backscattering cross-section may vary with the incidence angle (e.g., Leblond et al. 2014). This would influence flow rate measurements at the outer beams. In practical application, this effect should therefore be investigated by measuring the same bubble stream multiple times at different beam angles similar to the relative calibration described in 5.5. If a consistent dependency on the beam angle is found, it could be used to correct the measurements.

On using acoustically uncalibrated MBESs

For uncalibrated MBESs, each recorded echo level can be described using two (unknown) calibration factors.

$$\mathrm{EL}_{UC;pn,sn,bn} = \mathrm{EL}_{pn,sn,bn} - C_{\mathrm{Abs}} - C_{\mathrm{Rel}}(\vartheta) \tag{36}$$

where,

$\mathrm{EL}_{UC;pn,sn,bn}$	Received echo level for sample pn, sn, bn recorded by an uncalibrated system
C_{Abs}	Absolute calibration offset of the system (calibration offset of the center beam)
$C_{\mathrm{Rel}}(\vartheta)$	Relative calibration offset (compared to the center beam) of a beam pointing toward the across-track angle ϑ

Since the exact beam pattern and pulse shape are unknown for uncalibrated MBESs, the exact sample volume for computing $\tilde{s}_{V;pn,sn,bn}$ is also unknown. Combining Eqs. 36, 22, 14, and 3 reveals:

$$\tilde{s}_{V;pn,sn,bn} = 10^{\frac{\text{EL}_{\text{UC};pn,sn,bn} - \text{SL} + \text{TL}(R_{sn}) - 20\log(R_{sn})}{10}} \times 10^{\frac{C_{\text{Sv;Abs}}}{10}} \times 10^{\frac{C_{\text{Sv;Rel}}(\vartheta)}{10}} \quad (37)$$

$$C_{\text{Sv;Abs}} = C_{\text{Abs}} - 10\log\left(\Omega_{\text{TX}} \times \Omega_{\text{RX};0} \times c \times \frac{T_{\text{eff}}}{2}\right) \quad (38)$$

$$C_{\text{Sv;Rel}}(\vartheta) = C_{\text{Rel}}(\vartheta) - 10\log\left(\frac{\Omega_{\text{RX};bn=\vartheta}}{\Omega_{\text{RX};0}}\right) \quad (39)$$

where,

$C_{\text{Sv;Abs}}$	Absolute (center beam) calibration offset toward volume backscattering strength (includes the not perfectly known beam width and effective pulse length)
$C_{\text{Sv;Rel}}(\vartheta)$	Relative (compared to the center beam) calibration offset toward volume backscattering strength of a beam pointing toward the across-track angle ϑ
$\Omega_{RX;0}$	Beam width of center beam
$\Omega_{RX;bn=\vartheta}$	Receive beam width of a beam pointing toward the across-track angle ϑ

Note, for flat transducers, the size of the volumes typically increases by:

$$\frac{\Omega_{RX;bn=\vartheta}}{\Omega_{RX;0}} \approx \frac{1}{\cos(\vartheta)} \quad (40)$$

When gridding uncalibrated measurements using the proposed method, all voxel cells are equally influenced by the absolute calibration offset $C_{\text{Sv;Abs}}$. The influence of $C_{\text{Sv;Rel}}(\vartheta)$ on each voxel depends on the across-track angle of the measurements that contribute to the respective voxel value.

A relative calibration of the system means that the measurements are consistent for the different beam angles (Lurton et al. 2015). Using the echo grid integration, the factor $C_{\text{Sv;Rel}}(\vartheta)$ could be estimated by comparing $\tilde{\sigma}_{\text{AG;BL}}$ measurements of an isolated bubble stream of constant flow rate at different across-track angles. If this calibration can be achieved $(C_{\text{Sv;Rel}}(\vartheta) = 0)$, $C_{\text{Sv;Abs}}$ progresses linearly into Eq. 34. Thus, a direct calibration against bubble streams of known flow rates would allow to determine the factor $10^{-\frac{C_{\text{Sv;Abs}}}{10}}$ and thus calibrate uncalibrated $\tilde{\sigma}_{\text{AG;EWC}}$ values against gas flow rates.

Data availability statement

The simulation to reproduce the presented results, is published on doi:10.3289/SW_3_2023.

References

Ainslie, M. A., and T. G. Leighton. 2011. Review of scattering and extinction cross-sections, damping factors, and resonance frequencies of a spherical gas bubble. J. Acoust. Soc. Am. **130**: 3184–3208. doi:10.1121/1.3628321

Anderson, V. C. 1950. Sound Scattering from a Fluid Sphere. J. Acoust. Soc. Am. **22**: 426–431. doi:10.1121/1.1906621

Bayrakci, G., and others. 2014. Acoustic monitoring of gas emissions from the seafloor. Part II: a case study from the Sea of Marmara. Mar. Geophys. Res. **35**: 211–229. doi:10.1007/s11001-014-9227-7

Biastoch, A., and others. 2011. Rising Arctic Ocean temperatures cause gas hydrate destabilization and ocean acidification. Geophys. Res. Lett. **38**: L08602. doi:10.1029/2011GL047222

Boetius, A., and F. Wenzhöfer. 2013. Seafloor oxygen consumption fuelled by methane from cold seeps. Nature Geosci **6**: 725–734. doi:10.1038/ngeo1926

Campbell, K. A. 2006. Hydrocarbon seep and hydrothermal vent paleoenvironments and paleontology: Past developments and future research directions. Palaeogeogr Palaeoclimatol Palaeoecol **232**: 362–407. doi:10.1016/j.palaeo.2005.06.018

Clarke, J. E. H. 2006. Applications of multibeam water column imaging for hydrographic survey. Hydrogr. J **120**: 3–15.

Colbo, K., T. Ross, C. Brown, and T. Weber. 2014. A review of oceanographic applications of water column data from multibeam echosounders. Estuar. Coast. Shelf Sci. **145**: 41–56. doi:10.1016/j.ecss.2014.04.002

De Rosny, J., and P. Roux. 2001. Multiple scattering in a reflecting cavity: Application to fish counting in a tank. J. Acoust. Soc. Am. **109**: 2587–2597. doi:10.1121/1.1369101

Diner, N. 2001. Correction on school geometry and density: approach based on acoustic image simulation. Aquat, p. 12. doi: 10.1016/S0990-7440(01)01121-4

Diner, N. 2007. Evaluating uncertainty in measurements of fish shoal aggregate backscattering cross-section caused by small shoal size relative to beam width. Aquat. Living Resour. **20**: 117–121. doi:10.1051/alr:2007022

Dupré, S., C. Scalabrin, C. Grall, J.-M. Augustin, P. Henry, A. M. C. Şengör, N. Görür, M. N. Çağatay, and L. Géli. 2015. Tectonic and sedimentary controls on widespread gas emissions in the Sea of Marmara: Results from systematic, shipborne multibeam echo sounder water column imaging. J. Geophys. Res. Solid Earth **120**: 2891–2912. doi:10.1002/2014JB011617

Foote, K. G. 1983. Linearity of fisheries acoustics, with addition theorems. J. Acoust. Soc. Am. **73**: 1932–1940. doi:10.1121/1.389583

Gardner, J. V., M. Malik, and S. Walker. 2009. Plume 1400 meters high discovered at the seafloor off the Northern California Margin. Eos. Trans. AGU **90**: 275–275. doi:10.1029/2009EO320003

Global Carbon Project [WWW Document]. 2021. [accessed 2021 July 12]. Available from https://www.globalcarbonproject.org/.

Gorska, N., and D. Chu. 2005. On the echo interference in sound backscattering by densely aggregated targets. ICES J. Mar. Sci. **62**: 771–778. doi:10.1016/j.icesjms.2004.12.021

Greinert, J. 2008. Monitoring temporal variability of bubble release at seeps: The hydroacoustic swath system GasQuant. J. Geophys. Res. **113**: C07048. doi:10.1029/2007JC004704

Greinert, J., Y. Artemov, V. Egorov, M. Debatist, and D. Mcginnis. 2006. 1300-m-high rising bubbles from mud volcanoes at 2080m in the Black Sea: Hydroacoustic characteristics and temporal variability. Earth Planet. Sci. Lett. **244**: 1–15. doi:10.1016/j.epsl.2006.02.011

Holmin, A. J., N. O. Handegard, R. J. Korneliussen, and D. Tjøstheim. 2012. Simulations of multi-beam sonar echos from schooling individual fish in a quiet environment. J. Acoust. Soc. Am. **132**: 3720–3734. doi:10.1121/1.4763981

Holmin, A. J., R. J. Korneliussen, and D. Tjøstheim. 2016. Estimation and simulation of multi-beam sonar noise. J. Acoust. Soc. Am. **139**: 851–862. doi:10.1121/1.4941913

Hornafius, J. S., D. Quigley, and B. P. Luyendyk. 1999. The world's most spectacular marine hydrocarbon seeps (Coal Oil Point, Santa Barbara Channel, California): Quantification of emissions. J. Geophys. Res. **104**: 20703–20711. doi:10.1029/1999JC900148

ICES. 2021. Working Group of International Pelagic Surveys (WGIPS). ICES. doi:10.17895/ICES.PUB.8055

Jansson, P., B. Ferré, A. Silyakova, K. O. Dølven, and A. Omstedt. 2019. A new numerical model for understanding free and dissolved gas progression toward the atmosphere in aquatic methane seepage systems. Limnol. Oceanogr. Methods **17**: 223–239. doi:10.1002/lom3.10307

Kirschke, S., and others. 2013. Three decades of global methane sources and sinks. Nature Geosci. **6**: 813–823. doi:10.1038/ngeo1955

Leblond, I., C. Scalabrin, and L. Berger. 2014. Acoustic monitoring of gas emissions from the seafloor. Part I: quantifying the volumetric flow of bubbles. Mar. Geophys. Res. **35**: 191–210. doi:10.1007/s11001-014-9223-y

Leifer, I., J. R. Boles, B. P. Luyendyk, and J. F. Clark. 2004. Transient discharges from marine hydrocarbon seeps: spatial and temporal variability. Env. Geol. **46**: 1038–1052. doi:10.1007/s00254-004-1091-3

Leifer, I., D. Chernykh, N. Shakhova, and I. Semiletov. 2017. Sonar gas flux estimation by bubble insonification: application to methane bubble flux from seep areas in the outer Laptev Sea. Cryosphere **11**: 1333–1350. doi:10.5194/tc-11-1333-2017

Li, J., B. Roche, J. M. Bull, P. R. White, T. G. Leighton, G. Provenzano, M. Dewar, and T. J. Henstock. 2020. Broadband acoustic inversion for gas flux quantification—application to a methane plume at Scanner Pockmark, Central North Sea. J. Geophys. Res. Oceans **125**: e2020JC016360. doi:10.1029/2020JC016360

Lurton, X. 2010. An introduction to underwater acoustics: principles and applications, 2nd Edition. Springer.

Lurton, X., G. Lamarche, C. Brown, V. L. Lucieer, G. Rice, A. Schimel, and T. Weber. 2015. Backscatter measurements by seafloor-mapping sonars: guidelines and recommendations. http://geohab.org/wp-content/uploads/2014/05/BSWG-REPORT-MAY2015.pdf https://niwa.co.nz/static/BWSG_REPORT_MAY2015_web.pdf.

MacLennan, D. N. 1990. Acoustical measurement of fish abundance. J. Acoust. Soc. Am. **87**: 1–15. doi:10.1121/1.399285

Maclennan, D. N., P. G. Fernandes, and J. Dalen. 2002. A consistent approach to definitions and symbols in fisheries acoustics. ICES J. Mar. Sci. **59**: 365–369. doi:10.1006/jmsc.2001.1158

McGinnis, D. F., J. Greinert, Y. Artemov, S. E. Beaubien, and A. Wüest. 2006. Fate of rising methane bubbles in stratified waters: How much methane reaches the atmosphere. J. Geophys. Res. **111**: C09007. doi:10.1029/2005JC003183

Muyakshin, S. I., and E. Sauter. 2010. The hydroacoustic method for the quantification of the gas flux from a submersed bubble plume. Oceanology **50**: 995–1001. doi:10.1134/S0001437010060202

Nikolovska, A., H. Sahling, and G. Bohrmann. 2008. Hydroacoustic methodology for detection, localization, and quantification of gas bubbles rising from the seafloor at gas seeps from the eastern Black Sea. Geochem. Geophys. Geosyst. **9**: Q10010. doi:10.1029/2008GC002118

Ordoñez, A., I. Utseth, O. Brautaset, R. Korneliussen, and N. O. Handegard. 2022. Evaluation of echosounder data preparation strategies for modern machine learning models. Fish. Res. **254**: 106411. doi:10.1016/j.fishres.2022.106411

Ostrovsky, I. 2009. Hydroacoustic assessment of fish abundance in the presence of gas bubbles. Limnol. Oceanogr. Methods **7**: 309–318. doi:10.4319/lom.2009.7.309

Ostrovsky, I., D. F. McGinnis, L. Lapidus, and W. Eckert. 2008. Quantifying gas ebullition with echosounder: the role of methane transport by bubbles in a medium-sized lake. Limnol. Oceanogr. Methods **6**: 105–118. doi:10.4319/lom.2008.6.105

Padilla, A. M., S. Loranger, F. S. Kinnaman, D. L. Valentine, and T. C. Weber. 2019. Modern assessment of natural hydrocarbon gas flux at the coal oil point seep field, Santa Barbara, California. J. Geophys. Res. Oceans **124**: 2472–2484. doi:10.1029/2018JC014573

Pohlman, J. W., J. E. Bauer, W. F. Waite, C. L. Osburn, and N. R. Chapman. 2011. Methane hydrate-bearing seeps as a source of aged dissolved organic carbon to the oceans. Nature Geosci. **4**: 37–41. doi:10.1038/ngeo1016

Rehder, G., I. Leifer, P. G. Brewer, G. Friederich, and E. T. Peltzer. 2009. Controls on methane bubble dissolution

inside and outside the hydrate stability field from open ocean field experiments and numerical modeling. Mar. Chem. **114**: 19–30. doi:10.1016/j.marchem.2009.03.004

Riedel, M., F. Gausepohl, I.-Z. Gazis, L. Hähnel, M. Kampmeier, P. Urban, and J. Bialas. 2018. RV METEOR Fahrtbericht/Cruise Report M143: SLOGARO: Slope failures and active gas expulsion along the Romanian margin – investigating relations to gas hydrate distribution. GEOMAR Helmholtz-Zentrum für Ozeanforschung. doi:10.3289/GEOMAR_REP_NS_42_2018

Römer, M., S. Wenau, S. Mau, M. Veloso, J. Greinert, M. Schlüter, and G. Bohrmann. 2017. Assessing marine gas emission activity and contribution to the atmospheric methane inventory: A multidisciplinary approach from the Dutch Dogger Bank seep area (North Sea). Geochem. Geophys. Geosyst. **18**: 2617–2633. doi:10.1002/2017GC006995

Römer, M., H. Sahling, C. dos Santos Ferreira, and G. Bohrmann. 2020. Methane gas emissions of the Black Sea—mapping from the Crimean continental margin to the Kerch Peninsula slope. Geo-Mar. Lett. **40**: 467–480. doi:10.1007/s00367-019-00611-0

Sahling, H., and others. 2014. Gas emissions at the continental margin west of Svalbard: mapping, sampling, and quantification. Biogeosciences **11**: 6029–6046. doi:10.5194/bg-11-6029-2014

Scandella, B. P., L. Pillsbury, T. Weber, C. Ruppel, H. F. Hemond, and R. Juanes. 2016. Ephemerality of discrete methane vents in lake sediments. Geophys. Res. Lett. **43**: 4374–4381. doi:10.1002/2016GL068668

Schneider von Deimling, J., J. Greinert, N. R. Chapman, W. Rabbel, and P. Linke. 2010. Acoustic imaging of natural gas seepage in the North Sea: Sensing bubbles controlled by variable currents. Limnol. Oceanogr. Methods **8**: 155–171. doi:10.4319/lom.2010.8.155

Schneider von Deimling, J., and C. Papenberg. 2012. Technical Note: Detection of gas bubble leakage via correlation of water column multibeam images. Ocean Sci **8**: 175–181. doi:10.5194/os-8-175-2012

Schneider von Deimling, J., P. Linke, M. Schmidt, and G. Rehder. 2015. Ongoing methane discharge at well site 22/4b (North Sea) and discovery of a spiral vortex bubble plume motion. Mar Pet Geol **68**: 718–730. doi:10.1016/j.marpetgeo.2015.07.026

Shakhova, N., I. Semiletov, A. Salyuk, V. Yusupov, D. Kosmach, and Ö. Gustafsson. 2010. Extensive Methane Venting to the Atmosphere from Sediments of the East Siberian Arctic Shelf. Science **327**: 1246–1250. doi:10.1126/science.1182221

Shakhova, N., and others. 2014. Ebullition and storm-induced methane release from the East Siberian Arctic Shelf. Nature Geosci **7**: 64–70. doi:10.1038/ngeo2007

Simmonds, E. J., D. N. MacLennan, and D. N. MacLennan. 2005. Fisheries acoustics: theory and practice (Fish and aquatic resources series), 2nd Edition. Wiley-Blackwell.

Suess, E. 2018. Marine cold seeps: Background and recent advances, p. 1–21. *In* H. Wilkes [ed.], Hydrocarbons, oils and lipids: diversity, origin, chemistry and fate. Springer International Publishing. doi:10.1007/978-3-319-54529-5_27-1

Thuraisingham, R. A. 1997. New expressions of acoustic cross-sections of a single bubble in the monopole bubble theory. Ultrasonics **35**: 407–409. doi: 10.1016/S0041-624X(97)00021-8

Toresen, R. 1991. Absorption of acoustic energy in dense herring schools studied by the attenuation in the bottom echo signal. Fish. Res. **10**: 317–327. doi:10.1016/0165-7836(91)90083-R

Tréhu, A. M., J. Beeson, and S. G. Merle. 2021. A new approach to processing and imaging multibeam water column echosounder data: application to a complex methane seep on the southern Cascadia margin. Interpretation **1–47**: SB93–SB106. doi:10.1190/int-2021-0195.1

Turco, F., and others. 2022. Estimates of methane release from gas seeps at the Southern Hikurangi Margin, New Zealand. Front Earth Sci **10**. doi: 10.3389/feart.2022.834047

Urban, P., and E. Peschke. 2023. Multibeam echo grid simulator. GEOMAR Helmholtz Centre for Ocean Research Kiel, Germany. doi:10.3289/SW_3_2023

Urban, P., K. Köser, and J. Greinert. 2016. Processing of multibeam water column image data for automated bubble/seep detection and repeated mapping. Limnol Oceanogr Methods **15**: 1–21. doi:10.1002/lom3.10138

Urick, R. J. 1996. Principles of underwater sound, 3rd Edition. Peninsula Publ.

Veloso, M., J. Greinert, J. Mienert, and M. De Batist. 2015. A new methodology for quantifying bubble flow rates in deep water using splitbeam echosounders: Examples from the Arctic offshore NW-Svalbard: Quantifying bubble flow rates in deep water. Limnol. Oceanogr. Methods **13**: 267–287. doi:10.1002/lom3.10024

Veloso-Alarcón, M. E., P. Jansson, M. De Batist, T. A. Minshull, G. K. Westbrook, H. Pälike, S. Bünz, I. Wright, and J. Greinert. 2019. Variability of acoustically evidenced methane bubble emissions offshore Western Svalbard. Geophys. Res. Lett. **46**: 9072–9081. doi:10.1029/2019GL082750

Vielstädte, L., J. Karstens, M. Haeckel, M. Schmidt, P. Linke, S. Reimann, V. Liebetrau, D. F. McGinnis, and K. Wallmann. 2015. Quantification of methane emissions at abandoned gas wells in the Central North Sea. Mar. Pet. Geol. **68**: 848–860. doi:10.1016/j.marpetgeo.2015.07.030

Virtanen, P., and others. 2020. SciPy 1.0: fundamental algorithms for scientific computing in Python. Nat. Methods **17**: 261–272. doi:10.1038/s41592-019-0686-2

Weber, T. C. 2021. A CFAR detection approach for identifying gas bubble seeps with multibeam echo sounders. IEEE J. Oceanic Eng. **46**: 1346–1355. doi:10.1109/JOE.2021.3056910

Weber, T. C., L. A. Mayer, J. Beaudoin, K. Jerram, M. A. Malik, B. Shedd, and G. A. Rice. 2012. Mapping gas seeps with the

deepwater multibeam echosounder on okeanos explorer. Oceanography **25**: 54–55. doi:10.5670/oceanog.2011.supplement.01

Weber, T. C., L. Mayer, K. Jerram, J. Beaudoin, Y. Rzhanov, and D. Lovalvo. 2014. Acoustic estimates of methane gas flux from the seabed in a 6000 km2 region in the Northern Gulf of Mexico. Geochem. Geophys. Geosyst. **15**: 1911–1925. doi:10.1002/2014GC005271

Weidner, E., T. C. Weber, L. Mayer, M. Jakobsson, D. Chernykh, and I. Semiletov. 2019. A wideband acoustic method for direct assessment of bubble-mediated methane flux. Cont. Shelf Res. **173**: 104–115. doi:10.1016/j.csr.2018.12.005

Wilson, D. S., I. Leifer, and E. Maillard. 2015. Megaplume bubble process visualization by 3D multibeam sonar mapping. Mar Pet Geol **68**: 753–765. doi:10.1016/j.marpetgeo.2015.07.007

Xu, C., M. Wu, T. Zhou, J. Li, W. Du, W. Zhang, and P. R. White. 2020. Optical flow-based detection of gas leaks from pipelines using multibeam water column images. Remote Sens. (Basel) **12**: 119. doi:10.3390/rs12010119

Yamamoto, A., Y. Yamanaka, A. Oka, and A. Abe-Ouchi. 2014. Ocean oxygen depletion due to decomposition of submarine methane hydrate. Geophys. Res. Lett. **41**: 5075–5083. doi:10.1002/2014GL060483

Zhao, J., J. Meng, H. Zhang, and S. Wang. 2017. Comprehensive detection of gas plumes from multibeam water column images with minimisation of noise interferences. Sensors **17**: 2755. doi:10.3390/s17122755

Zwanzig, C. 2018. Ship-based exploration of submarine gas hydrates and environmental monitoring with multibeam echo sounders, p. 1–8. *In* 2018 OCEANS–MTS/IEEE Kobe Techno-Oceans (OTO). Presented at the 2018 OCEANS–MTS/IEEE Kobe Techno-Ocean (OTO). IEEE. doi:10.1109/OCEANSKOBE.2018.8559471

Conflict of Interest

None declared.